Summary of Research

User's Manual For

LINER: FORTRAN Code for the Numerical Simulation of Plane Wave Propagation in a Lined Two-Dimensional Channel

R.S. Reichert, S. Biringen and J.E. Howard

Department of Aerospace Engineering Sciences
University of Colorado, Boulder

April 7, 1999

LINER: Numerical Simulation of Plane Wave Propagation In A Lined Two-Dimensional Channel

User's Manual

R. S. Reichert, S. Biringen, and J. E. Howard

Aerospace Engineering Department, University of Colorado, Boulder, CO

April 7, 1999

1. Introduction

LINER is a system of Fortran 77 codes which performs a 2D analysis of acoustic wave propagation and noise suppression in a rectangular channel with a continuous liner at the top wall. This new implementation is designed to streamline the usage of the several codes making up LINER, resulting in a useful design tool. Major input parameters are placed in two main data files, *input.inc* and *num.prm*. Output data appear in the form of ASCII files as well as a choice of GNUPLOT graphs. Section 2 briefly describes the physical model. Section 3 discusses the numerical methods; Section 4 gives a detailed account of program usage, including input formats and graphical options. A sample run is also provided. Finally, Section 5 briefly describes the individual program files.

2. Physical Model

The physical model is based on the 2D compressible, inviscid fluid flow in a rectangular channel, as depicted in Fig. 1. We employ Cartesian coordinates (x, y), where x is the streamwise direction and y the normal direction. The governing equations are the 2D Euler equations,

$$Continuity: \quad \frac{\partial \rho}{\partial t} + \nabla \cdot (\rho \mathbf{V}) = 0$$

$$Momentum: \quad \rho\frac{\partial \mathbf{V}}{\partial t} + \rho\mathbf{V}\cdot\nabla\mathbf{V} = -\nabla p$$

$$Energy: \quad \frac{\partial E}{\partial t} + \nabla\cdot E\mathbf{V} = -\nabla\cdot(p\mathbf{V})$$

where $\mathbf{V} = (u,v)^T$ is the velocity, ρ is density, p is the pressure, and E is the total energy. These are numerically integrated, along with the equation of state,

$$E = \frac{p}{\gamma-1} + \frac{1}{2}\rho V^2$$

where γ is the ratio of specific heats, which we shall take as $\gamma = 1.4$. Nonreflective inflow and outflow boundary conditions are imposed. Boundary conditions at the normal walls $(y = \pm y_{max})$ are rigid slip, allowing nonzero tangential velocity while maintaining zero normal velocity. The initial conditions consist of a quiescent field, with an optional y-directed bias flow superimposed. Although this model is inviscid, a small artificial viscosity is used to stabilize the difference scheme.

The liner is incorporated as a source term in the momentum equations, rather than through boundary conditions. This is done semi-empirically, with impedance parameters chosen to match experimental data on the liner materials. As shown in Fig. 2, a steady bias flow through the liner is also modelled. See Ref. 1-2 for a detailed description of liner characteristics. Physically, the liner is composed of a face sheet and septum, sandwiching a honeycomb core. A constant bias velocity may be directed through the liner, if desired.

3. Numerical Method

The Euler equations are solved in space and time using the explicit (2,4) scheme of Gottlieb & Turkel [3], with artificial viscosity incorporated as a sixth-order source term. Spatial boundary conditions are implemented using the method of Thompson [4].

4. Computer Programs

4.1 General Description

LINER consists of a suite of F77 codes, which may be classified functionally as data input (relatively permanent or relatively ephemeral), computational, and data output (numerical or graphical). An entire program execution is supervised by a single Unix script, called RUN.

4.2 Input

Input parameters are found in *input.inc* and *num.prm*. The liner geometry is generated in *lnrgeom.f*, but the user need not edit this file. See section 4.5 (Sample Run) for the specific contents of the two input files.

4.3 Output

Sound pressure level is written to ASCII file *sound.idl*, while power per span is written to file *powspan*.

4.4 Graphical Options

All plotting is carried out in the GNUPLOT system, with a single Gnuplot macro processing a number of ASCII datafiles. Plots are automatically made (using GHOSTVIEW) of Transmitted Power per Span and Sound Pressure Level (SPL) y-profiles at three selected x-values. To page through plots, type in "q" after each plot. The four plots are written to files p1.ps, p2.ps, p3.ps, and p4.ps. The user may produce additional SPL profiles by running program *splx.f* with $x1$, $x2$, and $x3$ set as desired in *input.inc*.

4.5 Sample Run

As a specific case, let us consider a 61 cm × 19.25 cm domain, discretized by a 489 × 155 grid in x and y, i.e. $nx = 487$, $ny = 153$. With these choices, $dx = dy = 0.125$ cm. The lower liner sheet is located at y index $il = 122$, with upper sheet (septum) at $iu = 142$, corresponding to a total liner depth of 4 cm. The bias velocity, scaled by the sound speed, is negative blowing *out* of the liner. Here we take $v_{bias} = -0.01$. The equations are advanced a total of $nmx = 6000$ steps with timestep $dt = 0.02$. The input disturbance is a plane wave of nondimensional frequency $\omega = 0.23099946$ ($f = 1250$ Hz) and normalized amplitude $A = 0.002$ (140dB). Specifically, f is scaled by u_r/l_r, where u_r is sea level sound speed and $l_r = 1$ cm; A is scaled by $\rho_r u_r^2$, where ρ_r is sea level density. Parameters nmx, dx, and dt are to be specified by the user in file $num.prm$.

The liner impedance parameters (defined in Ref. 1) are specified by the user in file $input.inc$. This file also includes parameters dy, nx, ny, il, iu and v_{bias}. For this example, the liner impedance parameters were chosen to be $al = 0.0283$, $au = 0.0905$, $bl = 21.8$, $bu = 233.0$, $xclsp = -1.14$, and $xcusp = -1.11338$.

The Sound Pressure Level is to be plotted vs y at $x1 = 8.5$ cm, $x2 = 17.0$ cm, and $x3 = 52.5$ cm, as set in $input.inc$. SPL profiles may easily be generated for any other desired values of x without rerunning the whole code, by resetting x1,x2, and x3 in $input.inc$, then recompiling and executing $splx.f$. Figure 3 shows the resulting plot of Power Drop, while Fig. 4 presents the three SPL plots.

5. Glossary of Computer Programs

ff.f: Creates forcing function field to prevent the mean bias field from evolving in time. Writes file $ff.in$.

goplot: GNUPLOT macro to make plots of power drop and SPL.

4

input.inc: This is the basic input file, to be edited by the user. It is included in all FORTRAN codes.

linchn_orig.f: This is the workhorse of the system, which numerically solves the difference equations representing the flow.

linchn_ppav.f: Same as *linchn_orig.f*, except that time-averaging is applied to the fluctuating (acoustic) field. Writes final output files.

lnrgeom.f: Constructs liner forcing function distribution throughout domain.

mnbias.f: Creates solution field for any desired mean flow, such as a bias flow. Writes file *rstrt.in*.

num.prm: Contains basic run parameters, to be edited by the user. *Warning:* do not add any additional lines of comments to this file.

run: Unix script which supervises an entire run.

spl.f: Postprocessor to generate plot files for *goplot*

References

1. Reichert, R. S., Ph. D. Thesis, University of Colorado Dept. of Aerospace Engineering Sciences, 1998.

2. Reichert, R. S. and Biringen, S., *AIAA 97-1650* (1997).

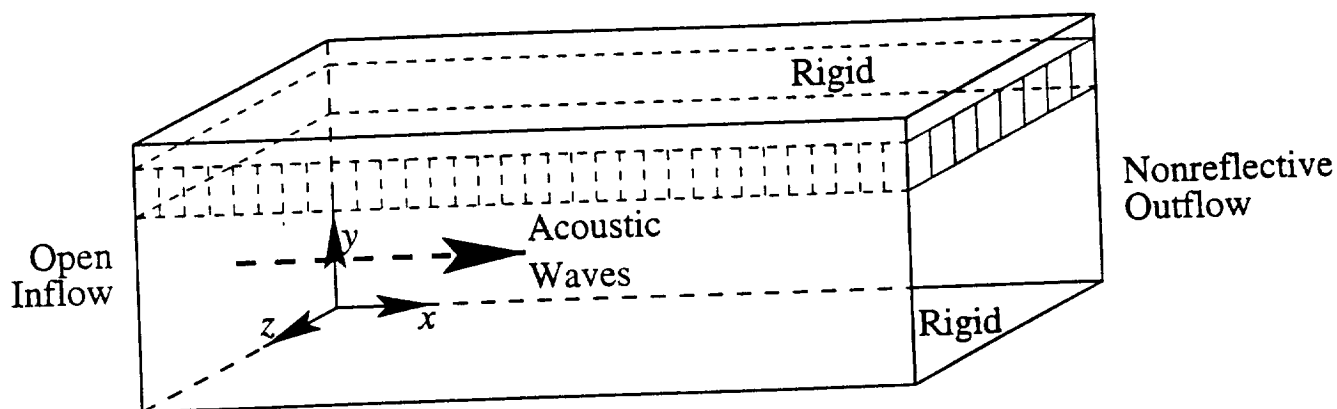3. Gottleib, D. and Turkel, E. *Math. Comp.* **115**, 43 (1976).

4. Thompson, K. W., *J. Comp. Phys.* **68**, 1 (1987).

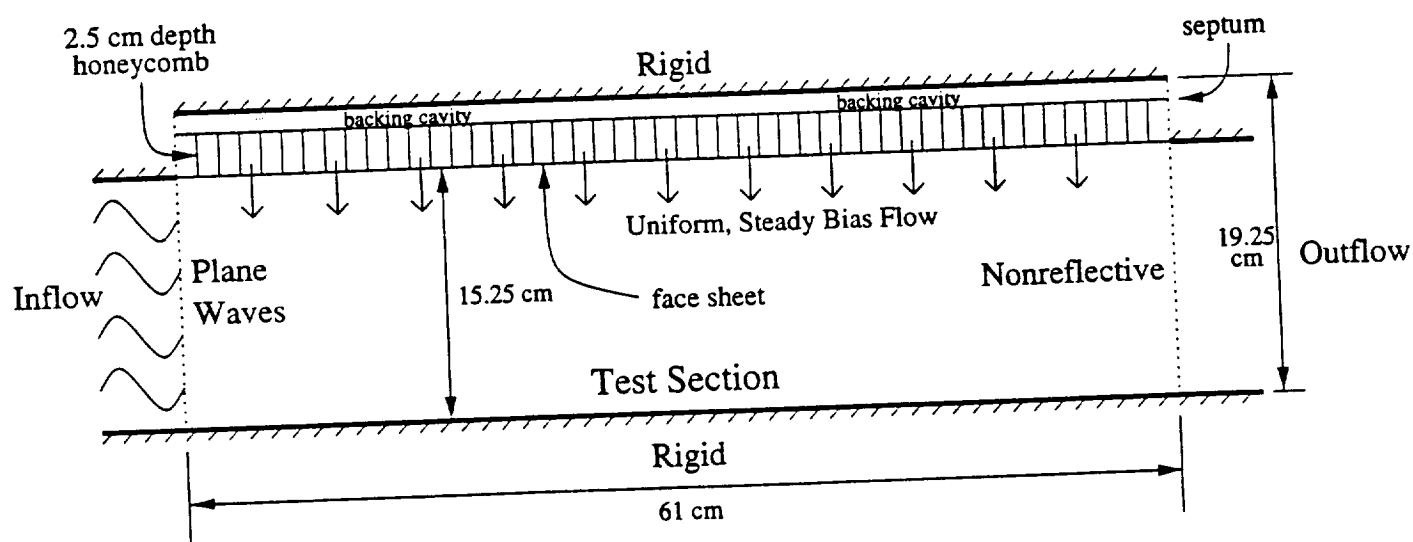Figure 1: Acoustic Channel Geometry.

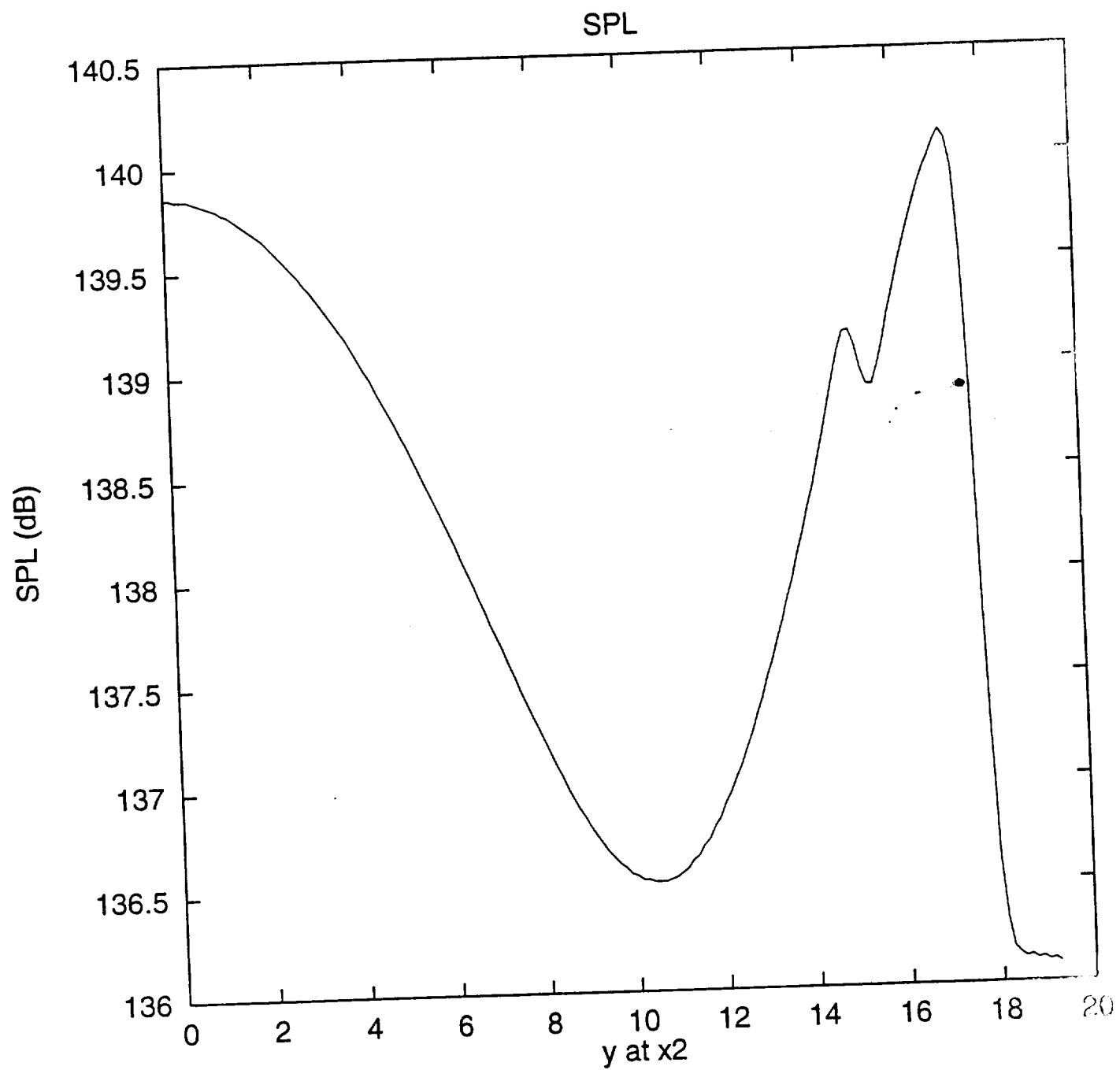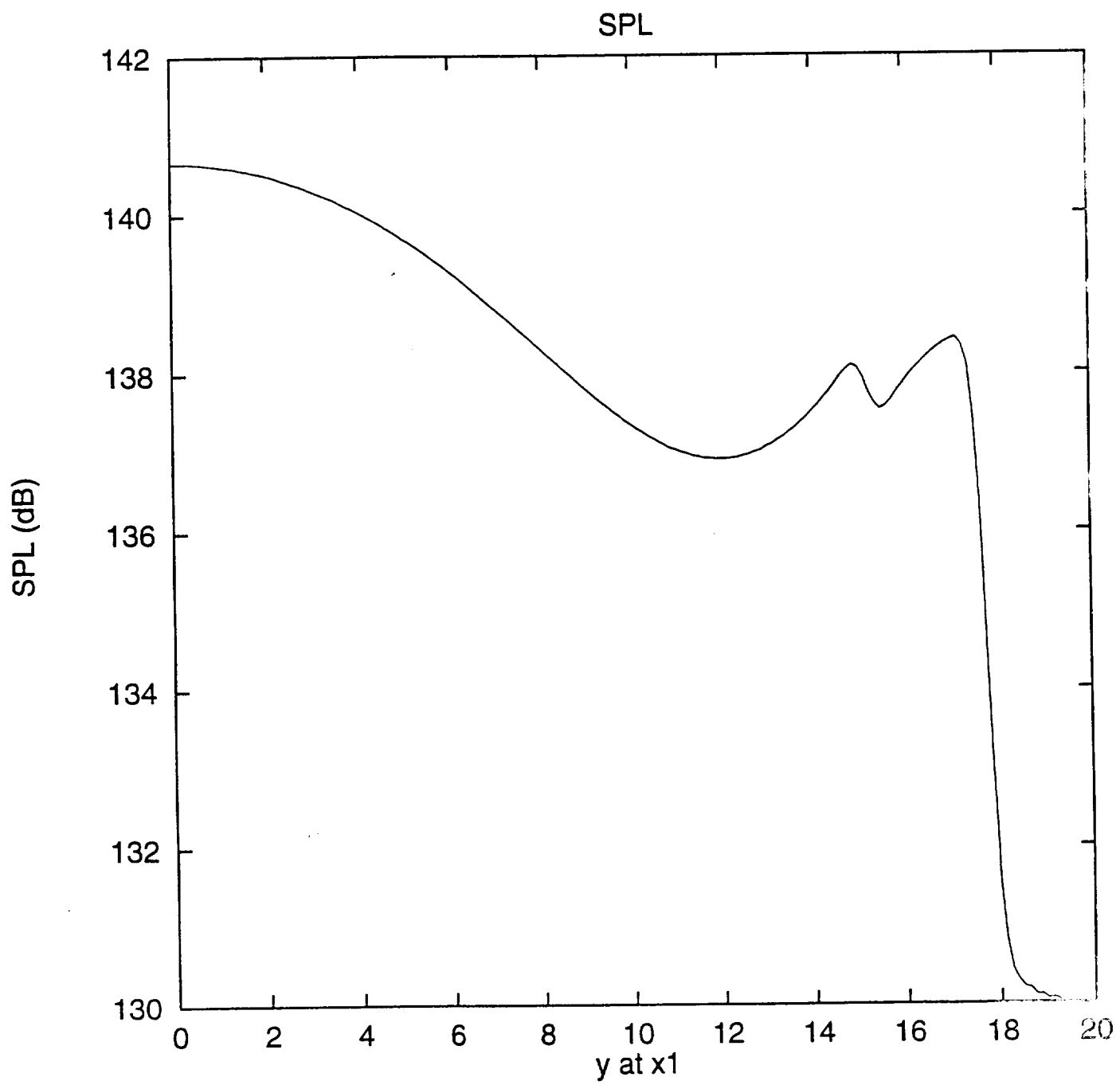Figure 2: Channel Geometry Employed in LINER Example.

SPL

y at x2

SPL

SPL (dB)

y at x1

Transmitted Power per Span

SPL

Plot of SPL (dB) versus y at x3. The vertical axis ranges from 120 to 136 dB and the horizontal axis ranges from 0 to 20.
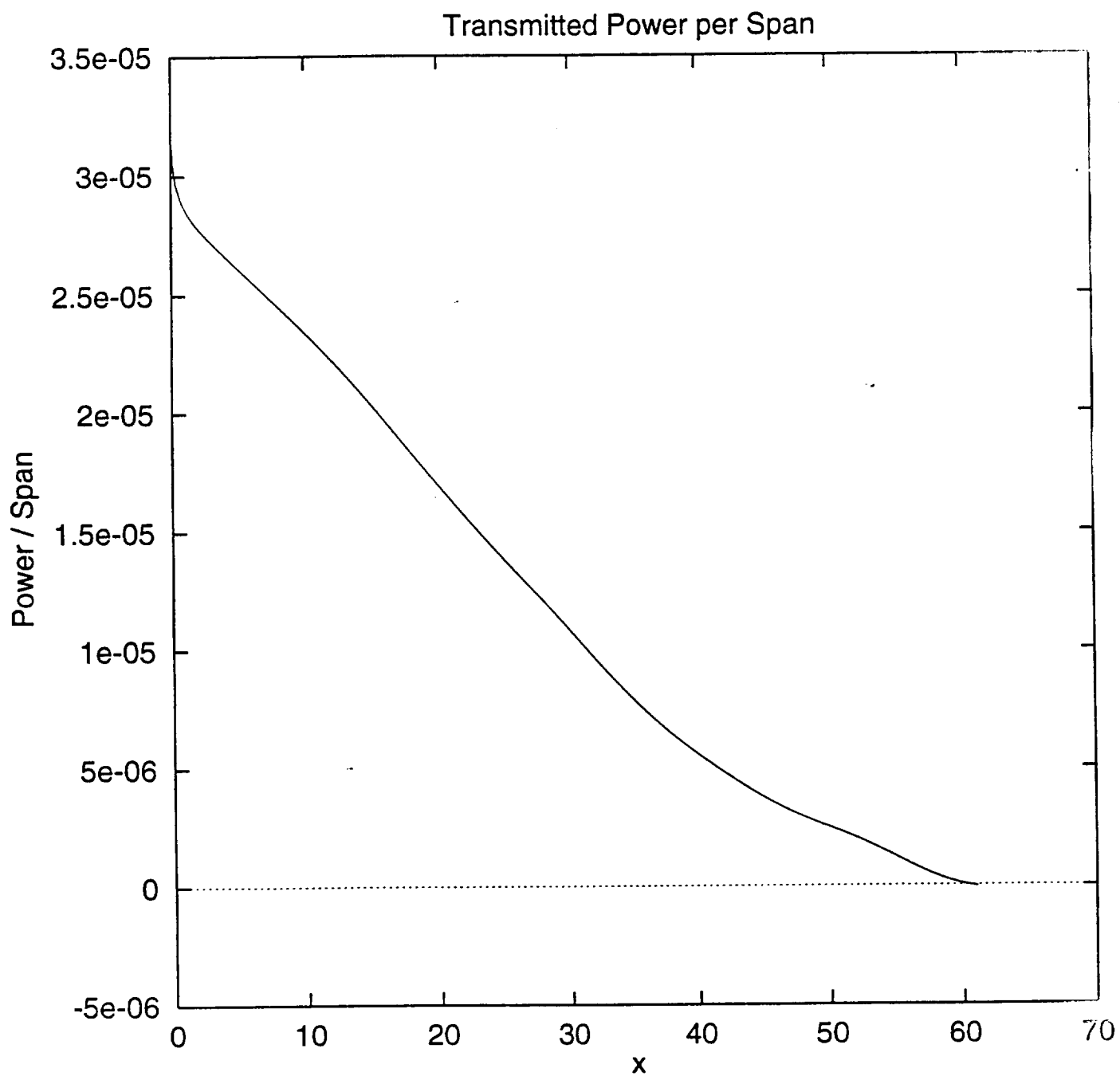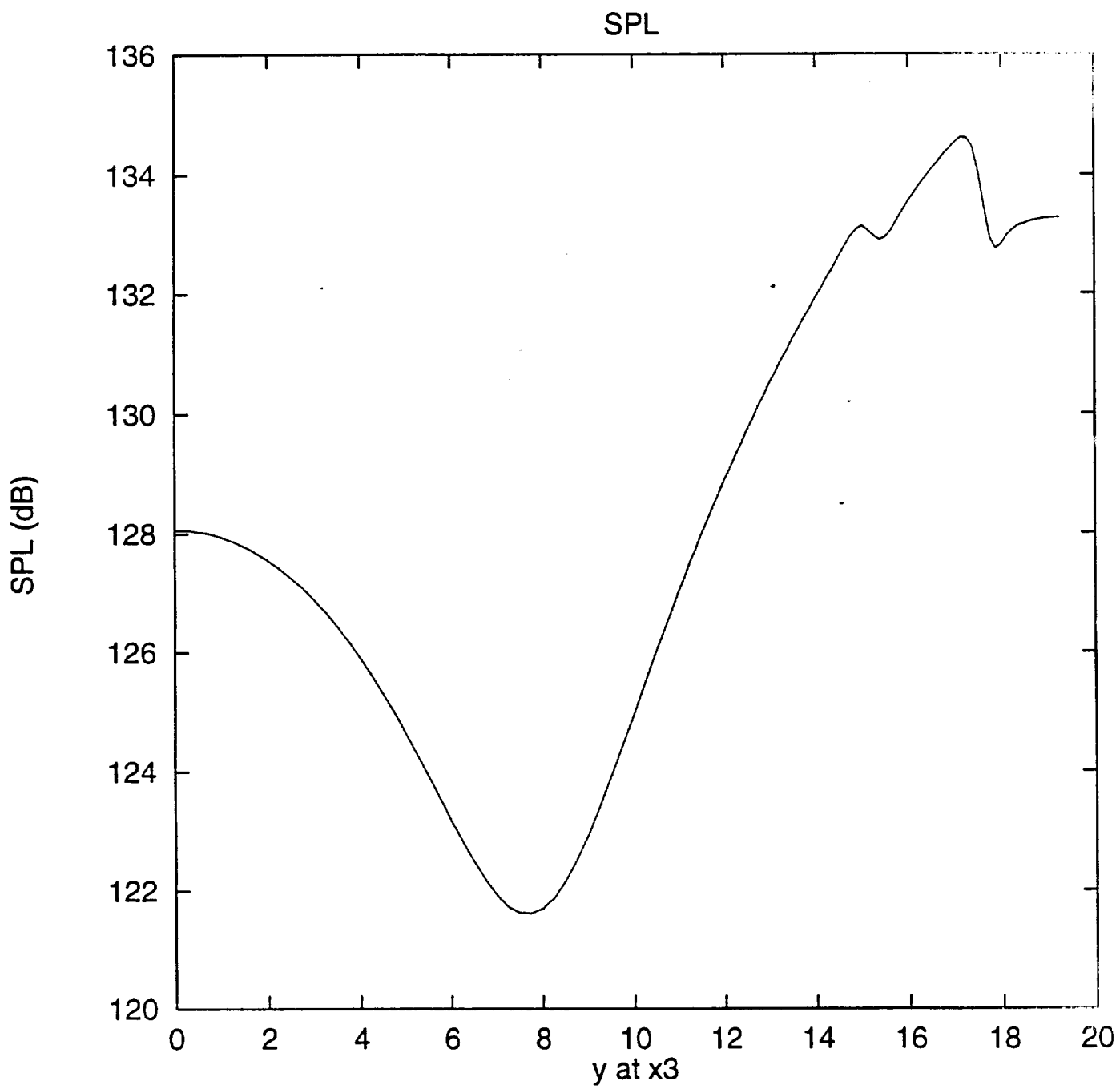
```
# Script to run LINER system
# Generate y-grid
# install test for files
rm newstrt.bin
rm grid.out
f77 -u grid.f -o gg
gg

f77 mnbias.f -o gmn
echo 'finished compiling grid.f and mnbias.f'
gmn
cp rstrt.0 rstrt.in
f77 lnrgeom.f -o gln
gln
f77 ff.f -o gff
gff
echo 'finished running lnrgeom.f and ff.f'
f77 linchn_orig.f -O2 -o gln
#f77 line.f -o gln
gln
echo 'finished running linchn_orig.f'
mv newstrt.bin rstrt.in
rm pp.av jetdat.bin jetgrd.bin
cp num.prm numsave.prm
echo 'starting addn'
f77 addn.f -o ga
ga
echo 'finished running addn'
mv nums.prm num.prm
gln
echo 'finished gln'
rm newstrt.bin jetdat.bin jetgrd.bin
f77 linchn_ppav.f -o gav
gav
echo 'finished running linchn_ppav.f'
cp num.prm numxx.prm
mv numsave.prm num.prm
f77 splx.f -o gg
gg
echo 'finished splx'
gnuplot goplot
```

```fortran
c      input.inc
c      Main input file, to be edited by the user.

c      grid constants (to be changed by user)

c      nx = number of interior x gridlines (nx+2 total, including boundaries)
c      ny = number of interior y gridlines (ny+2 total, including boundaries)
c      il = y index of lower porous sheet (face sheet)
c      iu = y index of upper porous sheet (septum)
c      dely = dx = dy = mesh spacing

       integer nx,ny,il,iu
       real dely
       parameter(nx=487,ny=153,dely = .125,il=122,iu=142)

c      physical constants (not to be changed)
       real gam,gam1
       parameter(gam=1.4, gam1 = 0.4)

c      rba and pba are quiescent medium nondim density and pressure
       real rba,pba
       parameter(rba=1.0,pba=0.714285714286)

c      Print interval
       integer npr
       parameter(npr = 100)

c      x-values for SPL plot (in cm)
       real x1spl,x2spl,x3spl
       parameter(x1spl = 8.5,x2spl = 17, x3spl = 52.5)

c      bias velocity
       real vbias
       parameter(vbias = -.01)

c      Liner Impedance Parameters
c      chc = honeycomb x resistive term
c      al = linear resistance term, lower porous sheet
c      bl = nonlinear resistance term, lower porous sheet
c      sg = sigma for resistance distribution
c      sgxl = sigma_x lower, lower sheet sigma for reactance distribution
c      sgxu = sigma_x upper, upper sheet sigma for reactance distribution
c      au = linear resistance term, upper porous sheet
c      bu = nonlinear resistance term, upper porous sheet
c      xclsp = lower sheet linearized reactance term
c      xcusp = upper sheet linearized reactance term

       real chc
       parameter(chc=0.8)
       real al,bl
       parameter(al=0.0283,bl=21.8)
       real sg,sgxl,sgxu
       parameter(sg = 2.0*dely,sgxl=2.*sg,sgxu=4.4*sg)
       real au,bu
       parameter(au=0.0905,bu=233.0)
       real xclsp
       parameter(xclsp=-1.14)
       real xcusp
       parameter(xcusp=-1.1338)
```

* variable rs is .true. if this is a restart and .false. if not
T

* variable nmx is the time step number to which to march
        6000

* variable ck is number of time steps between calls to chkval()
        100

* mean ic: =0 -> top-hat inflow (Not used in LINER)
        2

* variables dx (= dely = dy) ,dt

  0.1250000   2.0000000E-02

* level of sixth-order artificial dissipation vk
  2.0000000E-02

* constant in reflective outflow condition of Poinsot and Lele (subsonic only)
  0.0000000E+00

* nondimensional reference pressure for SPL calculation
  1.4100000E-10

* harmonic u disturbance amplitude and frequency
  2.0000001E-03   0.23099946

```fortran
      program splx.f

      generate SPL for gnuplot macro 'goplot'

      include 'input.inc'

      real xx(-1:nx+2),yy(-1:ny+1)

      real spl(0:nx+1,0:ny+1), y

      integer i,j,i1,i2,i3,n1,n2

      open(unit=35,file='sound',status='unknown')
      open(unit=351,file='splplot',status='unknown')

      read(35,*) n1,n2
      write(6,*) n1,n2

      do 100 j = 0,n2-1
      read(35,*)  (spl(i,j),i=0,n1-1)
100   continue

      i1 = x1spl/dely + .0000001
      i2 = x2spl/dely + .0000001
      i3 = x3spl/dely + .0000001

      write(351,98) x1spl,x2spl,x3spl
98    format('# x1 =',f8.5, ' x2 =',f8.5,'  x3 =',f8.5/)

      do 200 j = 0,n2-1
      y = j*dely
      write(351,99) y,spl(i1,j),spl(i2,j),spl(i3,j)
99    format(4e13.5)
200   continue

      close(35)
      close(351)

      end
```

```
# goplot (gnuplot macro)
set term postscript portrait
set samples 35000
set size .75, 1.
set autoscale
set nokey
#
set title 'Transmitted Power per Span'
set xlabel 'x'
set ylabel 'Power / Span '
set output 'p1.ps'
p 'powspan' w l
#
set title 'SPL'
set xlabel 'y at x1'
set ylabel 'SPL (dB)'
set output 'p2.ps'
p 'splplot' using 1:2 w l
#
set title 'SPL'
set xlabel 'y at x2'
set ylabel 'SPL (dB)'
set output 'p3.ps'
p 'splplot' using 1:3 w l
#
set title 'SPL'
set xlabel 'y at x3'
set ylabel 'SPL (dB)'
set output 'p4.ps'
p 'splplot' using 1:4 w l
#
!ghostview p1.ps
!ghostview p2.ps
!ghostview p3.ps
!ghostview p4.ps
q
```

TIME-DOMAIN SIMULATION OF
ACOUSTIC PROPAGATION IN A LINED DUCT

R.S. Reichert and S. Biringen Department of Aerospace Engineering Sciences
University of Colorado
Boulder, Colorado 80309-0429

Abstract

An inviscid, spatial time-domain numerical simulation is employed to compute acoustic wave propagation in a duct treated with an acoustic liner. The motivation is to assess the effects on sound attenuation of bias flow passed through the liner for application to noise suppression in jet engine nacelles. Physically, the liner is composed of porous sheets with backing air cavities. The mathematical model lumps the sheets' presence into a continuous empirical source term which modifies the right-hand side of the momentum equations. This source term specifies the time-domain characteristics of the frequency-domain resistance and reactance of the liner's component sheets. Nonlinear behavior of the liner sheets at high sound pressure levels is included in the form of the source term. The source term constants are empirically matched to frequency-domain impedance data via a one-dimensional numerical impedance tube simulation. The resulting liner model is then incorporated into a two-dimensional Euler solver and used for simulations of a realistic duct configuration. Sound pressure levels and axially transmitted power are computed to assess the attenuation effects of various magnitudes of bias flow. Simulation results are compared to available experimental data from a geometrically similar lined duct.

Problem Introduction and Description

Reduction of noise emitted from jet engines continues to be a key component of aircraft design. One major facet is inlet noise. Mechanical and hydrodynamic noise from the engine components propagates upstream and out of the inlet. Current generation jet engine designs treat nacelle inlets with acoustic liners composed of porous sheets with backing air cavities for acoustic attenuation. It

1

is well known that the impedance of porous sheets varies at high sound pressure levels. Observations show that incident sound pressure amplitude relates nonlinearly to particle velocity both for a single orifice (Ingard & Ising[1]) and porous sheets (Melling[2]). One concept for varying the impedance properties of liners is to exploit this nonlinear behavior by blowing a low level, steady bias flow through them. In this concept, the bias flow, which might be generated naturally by redirecting the oncoming air stream through the nacelle skin, can be adjusted to tune the liner impedance for optimal attenuation over a range of off-design flight conditions. The simulations presented in this work consider high amplitude acoustic propagation within a simple duct geometry in an effort to model the physics and eventually validate this idea.

We implement the liner model into the governing (Euler) equations through a source term in the interior of the computational domain. This approach enables the representation of complex composite liner structures in terms of one set of empirical, adjustable constants. An alternative way of representing the liner is advanced by Tam & Auriault,[3] where finite impedance *boundary conditions* are imposed at the liner surface. However, because this model requires composite liner impedance information at the boundary, it can be difficult to model complex liners. In the present liner model, we lump the physical and geometric attributes of the liner into a source term in the momentum equations. This source term is frequency-independent and contains several empirical constants which are matched to impedance data (obtained in the frequency-domain), for a given liner component. Consequently, the time-domain model so obtained produces the same impedance behavior as the actual material. In this way, complex lining geometries, composed of multiple sheets with various impedances, can be built up with ease, in contrast to boundary condition methods which must know the liner's *composite* impedance presented to the duct at the face sheet. The governing equations are integrated forward in time to capture the evolution of the acoustic field in the presence of the liner structure. The primary motivation is to assess and optimize the effect of natural bias flow through the liner.

The geometry considered here approximates that of a lined duct test section constructed at Rohr, Inc., as detailed by Yu, Kwan, & Stockham.[4] Depicted in Fig. 1, the section is 19.25 *cm*

2

in height and 61 *cm* in length. The numerical simulation considers a two-dimensional planar cut bounded by solid rigid walls at top and bottom and by open boundaries, indicated by dotted lines in the figure, at left and right. The experiment also possessed upstream and downstream hard walled duct extensions with reverberation chamber terminations; the present simulations include only the test section. The top surface of the duct is acoustically treated with a liner composed of a porous face sheet (18% open area) and backing septum (6% open area) sandwiching a honeycomb core. Plane waves (i.e., lowest duct mode) are forced at the left boundary and allowed to propagate along the duct to the right through a quiescent air medium. Although only plane wave cases are reported here, the method allows examination of higher duct modes simply by changing the form of the time-dependent forcing applied at the left boundary.

As implemented in the present study, time-domain modeling of acoustic lining materials has several advantages over frequency-domain analysis. First, it provides a convenient means of implementing complex liner structure. Composite liners of any number of sheets and backing cavities may be built up. As mentioned above, only the component impedance of the sheets, rather than the composite impedance at the face sheet, need be known. It is also simple to construct liners in which impedance varies spatially, which is useful since segmented treatment allows attenuation of widely disparate frequencies (Motsinger & Kraft[5]). Another strength of the current model is that it accommodates both linear and nonlinear noise amplitudes and incorporates nonlinear impedance of the porous sheets. Finally, time-domain analysis may treat multiple frequencies and acoustic modes simultaneously. These many desirable qualities make time-domain analysis attractive for computational aeroacoustic problems.

Development of Time-Domain Model Form

Our goal is to develop governing equations for a continuum which contains porous material. While no universal form exists for the equations governing flow through porous media (Nayfeh, Kaiser, & Telionis[6]), Morse & Ingard[7] provide a widely accepted form. The discussion below justifies, to some degree, the form of their momentum conservation equations. Mass and energy conservation equations could have analogous modifications. However, numerical impedance tube

3

experiments, similar to those discussed below, reveal that the appropriate mass conservation modification produces only infinitesimal differences in results. Energy conservation plays only a passive role in acoustics, so its modifications are neglected here as well. Consequently, we treat only momentum conservation.

We consider the equations for conservation of momentum, which apply for a compressible, viscous flow:

$$\frac{\partial}{\partial t}(\rho u_i) + \frac{\partial}{\partial x_j}(\rho u_i u_j) = \frac{\partial \tau_{ij}}{\partial x_j}, \tag{1}$$

for $i = 1, 2, 3$. Here, τ_{ij} is the stress tensor which includes stress due to pressure. Suppose that porous acoustic lining material is distributed uniformly in some region of the flow field. The material's presence will cause flow resistance which can be modeled as as normal stress term across an infinitesimal fluid volume in each coordinate direction. This term augments the pressure gradient as shown in Fig. 2. Consequently, denoting acoustic material resistance as N, we modify the stress term to read

$$\tau_{ij} = -(p + N)\delta_{ij}. \tag{2}$$

Here, we have assumed that the porous material imparts no net shear to the fluid. Following Zorumski & Parrott,[8,9] we write the gradient of N as a time-domain damping term R_{td} multiplied by the local velocity u_i, so that

$$\frac{\partial \tau_{ij}}{\partial x_j} = -\frac{\partial p}{\partial x_i} - R_{td} u_i. \tag{3}$$

Additionally, the effective fluid density within the volume is increased by a constant time-domain factor X_{td} (typically between 1.5 and 5.0 for acoustic materials[7]) due to the material's presence:

$$\rho \longrightarrow X_{td}\rho \qquad X_{td} \geq 1. \tag{4}$$

The density factor accounts for an increase in effective mass as the fluid moves through constrictions, as suggested by Morse & Ingard.[7] Substituting Eq. (3) into Eq. (1) and making the replacement (4) yields a modified differential momentum equation:[7]

$$\frac{\partial}{\partial t}(\rho u_i) + \frac{\partial}{\partial x_j}(\rho u_i u_j) = -\frac{1}{X_{td}}\left(\frac{\partial p}{\partial x_i} + R_{td} u_i\right). \tag{5}$$

4

We must now substitute model relations for R_{td} and X_{td} which properly represent the time-domain behavior of acoustic lining materials. This is accomplished by using forms which reproduce the porous material behavior in the proximity of each component porous sheet, as elaborated in the following section.

Mathematical Model

The full governing equations are the two-dimensional Euler equations, which express conservation of mass, momentum, and energy for the inviscid motion of compressible fluids. They are here written for a cartesian domain:

$$\frac{\partial \vec{W}}{\partial t} + \frac{\partial \vec{F}}{\partial x} + \frac{\partial \vec{G}}{\partial y} = \vec{S}, \tag{6}$$

where

$$\vec{W} = (\rho \quad \rho u \quad \rho v \quad E)^{\mathrm{T}}, \tag{7}$$

and

$$\vec{F} = \begin{pmatrix} \rho u \\ \rho u^2 \\ \rho v u \\ [E+p]u \end{pmatrix}, \qquad \vec{G} = \begin{pmatrix} \rho v \\ \rho u v \\ \rho v^2 \\ [E+p]v \end{pmatrix}. \tag{8}$$

The state equation closes the system:

$$E = \frac{p}{\gamma - 1} + \frac{1}{2}\rho(u^2 + v^2). \tag{9}$$

The above set has, as the dependent variables, the conserved quantities of mass ρ, x-directed momentum ρu, y-directed momentum ρv, and total energy E, each expressed on a per volume basis. The primitive variables are density ρ, x-directed velocity u, y-directed velocity v, and pressure p. Note that $\vec{S}$ is the right-hand side term of Eq. (5). Specification of the open sides as nonreflective and the solid walls as rigid slip boundaries in Fig. 1 completes the definition of the mathematical problem.

We have nondimensionalized the equation system using the following reference scales:

$$l_r = 0.01 \ m \longrightarrow \text{length scale,}$$
$$U_r = 340.25 \ m/s \longrightarrow \text{velocity scale,}$$
$$l_r/U_r = 2.939 \times 10^{-5} \ s \longrightarrow \text{time scale,}$$
$$\rho_r = 1.225 \ kg/m^3 \longrightarrow \text{density scale,}$$
$$\rho_r U_r^2 = 1.418 \times 10^5 \ Pa \longrightarrow \text{pressure, energy scale.}$$

Note that the density and velocity reference values correspond to standard atmosphere density and sound speed. It is also worth noting that the equations will capture both linear and nonlinear phenomena, which is important for high amplitude wave dynamics.

The presence of the discrete porous sheets is felt via the source term $\vec{S}$ which comes from the right hand side of Eq. (5). We form R_{td} and X_{td} to capture the general experimental frequency-domain behavior observed by Ingard & Ising,[1] Melling,[2] and Zorumski & Parrott.[9] Specifically, Rohr, Inc. provided impedance data in the form:

$$z = (\mathcal{R}_0 + SV) + i\mathcal{X}, \tag{10}$$

where V is the root-mean-square particle velocity at the sheet surface. The real part is the velocity dependent resistance, and the imaginary part is the reactance. Reactance is frequency dependent and was provided as

$$\mathcal{X} = mk,$$

where k is the incident wavenumber and m is a given constant for each porous sheet type. The term $\vec{S}$ (the right-hand side of Eq. (5)) allows for simple nonlinear behavior in the resistance. For R_{td}, we use

$$R_{td} = f_R(x,y)(A + B|u_i|),$$

where $u_i = u, v$ for the x and y momentum equations, respectively. The function $f_R(x,y)$ is a smearing function meant to distribute the discrete effect of a porous sheet. It is introduced purely for numerical convenience and is detailed below. Similarly, we substitute a model for X_{td} in $\vec{S}$:

$$X_{td} = 1 - X(f_X(x,y)/[f_X(x,y)]_{\max}).$$

6

Here again, we have introduced a convenient smearing function, this time $f_X(x,y)$. Once R_{td} and X_{td} are specified, we can detail the entire right-hand side source term $\vec{S}$:

$$\vec{S} = -\frac{1}{1 - X(f_X(x,y)/[f_X(x,y)]_{\max})} \begin{pmatrix} 0 \\ [\partial p/\partial x + u f_R(x,y)(A + B|u|)] \\ [\partial p/\partial y + v f_R(x,y)(A + B|v|)] \\ 0 \end{pmatrix} - \begin{pmatrix} 0 \\ u\, C(x,y) \\ 0 \\ 0 \end{pmatrix}. \quad (11)$$

The velocities u and v are the same particle velocities present in the terms $\vec{W}$, $\vec{F}$, and $\vec{G}$ defined by Eqs. (7) and (8) and contain the bias flow velocity. In effect, the empirical parameters A, B, and X, respectively, specify the levels of linear resistance, nonlinear resistance, and linear reactance of each sheet, but in the time-domain. The distribution $C(x,y)$ is set to a constant value ($C = 0.8$) between the face sheet and parallel backing septum to account for the presence of the honeycomb core. Since this additional resistance-like term only appears in the x-momentum equation, it acts to suppress u within the core and thus helps the face sheet/septum combination approximate a locally reacting liner element. Note that $A = B = C = X = 0$ gives back the original Euler equations, so these correspond to open air.

As discussed above, the functions $f_R(x,y)$ and $f_X(x,y)$ control the spatial distribution of the liner's effect for the resistance and reactance, respectively. They are specified as Gaussian distributions in a coordinate s normal to the sheet surfaces:

$$f(s) = \frac{1}{\sigma}\frac{1}{\sqrt{2\pi}} e^{-s^2/2\sigma^2}. \quad (12)$$

Within these functions, σ determines the distribution thickness, so we have σ_R and σ_X, respectively, for $f_R(x,y)$ and $f_X(x,y)$. The constant σ_R is fixed as $2\Delta x$ simply to distribute the discrete effect of sheet resistance for numerical purposes. The constants A, B, X, and σ_X are matched to complex impedance data via a numerical impedance tube simulation, as described below. The authors conducting the duct experiment[4] provided the impedance data. The above model has a simple nonlinear behavior in analogy to Eq. (10), but there is no inherent limitation to the complexity that could be mimicked with the time-domain model.

7

Nonlinear behavior in reactance is not explicitly modeled in Eq. (11), though it is physically present. The model consequently linearizes the reactance about each particular bias flow level. Nonlinearity tends to reduce the sheet reactance, but the effect is not indefinite as acoustic amplitude increases. When the root-mean-square normal velocity at the sheet surface attains a high level, the reactance assumes a constant value. The velocity at which this saturation occurs depends on the particular sheet porosity, but is at most $V = 0.0095$ for the component sheets considered here. A *constant* reactance must consequently be used for all sheets when $|v_{\text{bias}}| \geq 0.0095$. Below this level, each sheet is considered separately as to whether its reactance behaves nonlinearly or is saturated. This means that $\mathcal{X}$ in Eq. (10) is a somewhat complicated function of V. To approximate the variable reactance, X is consequently computed to be a fixed number between the linear X_{max} and the saturated X_{min}, sized according to the expected normal velocity at each sheet surface.

Numerical Solution Method

We discretize and numerically integrate the partial differential equation system Eq. (6), coupled with the spatial boundary conditions, in a rectangular domain, with a uniform mesh in both the x- and y-directions. The time-advancement scheme is Gottlieb & Turkel's[10] explicit (2,4) scheme, which is second-order accurate in time and fourth-order in space. The variant of the method used here is a MacCormack-like explicit predictor/corrector. For grids that are uniform in x and y, the method may be written as:

$$
\begin{aligned}
\vec{W}_{i,j}^{*} &= \vec{W}_{i,j}^{n} \\
&\quad - \lambda_x [7(\vec{F}_{i+1,j}^{n} - \vec{F}_{i,j}^{n}) - (\vec{F}_{i+2,j}^{n} - \vec{F}_{i+1,j}^{n})] \\
&\quad - \lambda_y [7(\vec{G}_{i,j+1}^{n} - \vec{G}_{i,j}^{n}) - (\vec{G}_{i,j+2}^{n} - \vec{G}_{i,j+1}^{n})] \\
&\quad + \Delta t(\vec{D}_{i,j}^{n}) + \Delta t(\vec{S}_{i,j}^{n}), \\
\vec{W}_{i,j}^{n+1} &= \frac{1}{2}\Big\{ \vec{W}_{i,j}^{n} + \vec{W}_{i,j}^{*} \\
&\quad - \lambda_x [7(\vec{F}_{i,j}^{*} - \vec{F}_{i-1,j}^{*}) - (\vec{F}_{i-1,j}^{*} - \vec{F}_{i-2,j}^{*})] \\
&\quad - \lambda_y [7(\vec{G}_{i,j}^{*} - \vec{G}_{i,j-1}^{*}) - (\vec{G}_{i,j-1}^{*} - \vec{G}_{i,j-2}^{*})]
\end{aligned}
\tag{13}
$$

8

$$+\Delta t(\vec{D}_{i,j}^{*}) + \Delta t(\vec{S}_{i,j}^{*})\bigg\}. \tag{14}$$

Here,

$$\lambda_x = \frac{\Delta t}{6\Delta x}, \qquad \lambda_y = \frac{\Delta t}{6\Delta y}.$$

The spatial derivatives of pressure in $\vec{S}$ are computed using second-order central finite differences. The above steps employ forward differencing in the predictor step and backward differencing in the corrector step. This is switched on alternating time steps to a predictor with backward differencing and corrector with forward differencing to obtain the full (2,4) accuracy. For stability, the Courant-Friedrichs-Lewy (CFL) number is made to satisfy:

$$\text{CFL}_x = \frac{(u+a)_{\max}\Delta t}{\Delta x} < \frac{2}{3},$$

and

$$\text{CFL}_y = \frac{(v+a)_{\max}\Delta t}{\Delta y} < \frac{2}{3},$$

where a is the local sound speed, $a = \sqrt{\gamma p/\rho}$.

The (2,4) stencil has five points in both x- and y-directions, so it extends over the domain edges at a boundary and first interior point. The method uses the unmodified (2,4) scheme at the first interior point. To account for the point beyond the edge, fluxes are extrapolated (third-order) to a ghost point one increment outside the domain. Boundary points, including both rigid top and bottom walls and the nonreflective boundaries at the "inflow" and "outflow", are treated with the method of Thompson.[11,12] This boundary treatment uses a characteristic decomposition of the Euler equations to give an estimate of the flux derivative normal to the boundary at the boundary. The method works well with the plane wave modes considered in the present problem, as elaborated in the code validation presented below.

Artificial viscosity terms are added to the numerical scheme to enhance stability, as indicated by the $\vec{D}$ terms. Sixth-order dissipation is added as a source term to the right-hand side of the Euler equations:

$$\vec{D} = \epsilon_d\left((\Delta x)^6\frac{\partial^6\vec{W}}{\partial x^6} + (\Delta y)^6\frac{\partial^6\vec{W}}{\partial y^6}\right). \tag{15}$$

The magnitudes of the artificial viscosity terms are $O[(\Delta x)^6]$ and $O[(\Delta y)^6]$, so the fourth-order spatial accuracy of the method is unaffected. The parameter ϵ_d is empirically defined and did not exceed $\epsilon_d = 0.04$. The central difference coefficients used for the sixth-derivatives are computed using Lagrange polynomials. We found some explicit dissipation necessary to suppress spurious oscillations developing around the porous sheets.

The mean bias flow is specified as a "frozen" field upon which the acoustic perturbations are allowed to evolve. In this way, the mean field need not be computed; nor does it evolve. The addition of a forcing term $\vec{\varepsilon}$ to Eq. (6) accomplishes this:

$$\frac{\partial \vec{W}}{\partial t} + \frac{\partial \vec{F}}{\partial x} + \frac{\partial \vec{G}}{\partial y} - \vec{S} + \vec{\varepsilon} = 0, \tag{16}$$

where

$$\vec{\varepsilon} = -\frac{\partial \overline{\vec{F}}}{\partial x} - \frac{\partial \overline{\vec{G}}}{\partial y} + \overline{\vec{S}}. \tag{17}$$

The overbar here denotes the base field, which consists of the bias flow and grazing flow (if present) but *not* the acoustic perturbations. A uniform vertical velocity v_{bias} is used throughout the domain for the base field. Thus, the bias is directed normal to the liner, and there is no grazing flow. For the relatively low bias flow levels of the present study, there is physically no significant coupling between acoustic and mean flow fields, so this frozen flow technique is expected to be valid. It should also be noted that a bulk grazing flow in the duct could be implemented using such a frozen flow formulation. The technique has the limitation that the mean flow field does not feel the presence of the liner structure, but it is a quick way to obtain a converged bias flow.

Numerical Impedance Tube Simulation

As mentioned above, the liner model's parameters must be matched to the *a priori* known impedance data for the component porous sheets under consideration. To this end, a numerical model for an impedance tube is developed. In this model, one-dimensional Euler equations are integrated on a domain with a rigid termination at the right end, and the left boundary is forced with acoustic waves. A numerical porous sheet "sample" is placed some distance to the left of the rigid termination by centering the Gaussian distributions Eq. (12) at that point. The effective

10

impedance of the sample is deduced from the standing wave pattern set up by the incident and reflected waves.

The impedance tube computations employ parameters similar to those used in the full two-dimensional simulations. For instance, $\Delta x = 0.125$ and $\Delta t = 0.025$. The acoustic forcing at the left boundary of the form:

$$\bar{p}(t) = P\cos(\omega t + \pi/2) \quad \bar{u} = \bar{p} \quad \bar{v} = 0 \quad \bar{\rho} = \bar{p}, \tag{18}$$

gives purely plane waves with nondimensional wavelength 25, which is also the temporal period. This corresponds to 1361 Hz, a value within the frequency range of interest for the two-dimensional duct. The domain has 601 points so that the tube length is 75. The simulations are run $5500\Delta t$, or to nondimensional time 137.5. This allows waves propagating at unity sound speed to set up several wavelengths of a standing wave without the reflected wave impacting the left boundary.

We follow the method of Kinsler, Frey, Coppens, & Sanders[13] to extract the impedance from the standing wave pattern. Accordingly, the impedance z is computed as

$$z = \frac{1 + Ke^{i\theta}}{1 - Ke^{i\theta}}. \tag{19}$$

The constant K is given in terms of the standing wave ratio SWR, the ratio of maximum to minimum pressure amplitude:

$$K = \frac{\text{SWR} - 1}{\text{SWR} + 1}, \quad \text{where} \quad \text{SWR} = \frac{P_{\max}}{P_{\min}}. \tag{20}$$

The phase of the standing waves relative to the sample surface determines θ:

$$\theta = 2k(x_{\text{sample}} - x_{\text{node}}) - \pi, \tag{21}$$

where k is the wavenumber of the incident waves. (Refer to Fig. 3 for an example of these quantities as measured from a standing wave pattern.) The impedance value thus measured equals that of the sample plus the impedance of the closed tube behind the sample. Kinsler et al.[13] show that this backing tube impedance is $-\cot(kd)$, where d is the depth of the cavity from the sample to the rigid termination. Consequently, we fix the depth at one-quarter incident wavelength such that $-\cot(kd) = 0$, and the measured impedance is simply that of the sample.

11

Porosity	A	B	$X_{\max}$	$X_{\min}$	σ_X
18%	0.0283	21.8	-0.738	-0.570	4.0 Δx
6%	0.0905	233	-0.908	-0.669	8.8 Δx

Table 1: Time-Domain Model Parameters for Liner's Component Porous Sheets

Equation (10) represents the frequency-domain impedance, and components $\mathcal{R}_0$, $\mathcal{S}$, and $\mathcal{X}$ are experimentally determined for a given liner material such that they are known input for matching to our time-domain model. The time-domain constants A, B, X, and σ_X are adjusted until the computed impedance matches that of the porous sheet, given in the form of Eq. (10). In matching, there exists a one-to-one correspondence between A and $\mathcal{R}_0$, B and $\mathcal{S}$, and X and $m = \mathcal{X}/k$. The parameter σ_X may also be adjusted to effect gross changes in $m = \mathcal{X}/k$. It should be noted that X and σ_X, since they match to m for any wavenumber k, are usable time-domain constants regardless of the incident frequency. When computing total (linear plus nonlinear) resistance, V is computed in the simulation as the root-mean-square velocity over one wave period at the center of the sheet distribution. Figure 3 shows a representative standing wave solution for the 6% open sheet, with the center of the sheet indicated by the vertical line. Table 1 displays the constants obtained through application of this method to the three sheet types. This method is general in the sense that complex impedance data for any sample, porous sheet or other, can be matched to the empirical constants of the model.

By matching the frequency-domain data to time-domain parameters, we have ensured that the numerical "sample" possesses the correct time-domain behavior. Figure 4 provides an additional qualitative validation. The plot shows the Fourier transform of a pressure time series recorded at a point midway between the sample and the rigid termination in the impedance tube. This particular case employs parameters for a 6% porous sample. It is apparent that the sound pressure transmitted through the sample contains overtones of the fundamental almost entirely of odd order. This effect is characteristic of material with nonlinear impedance and has been observed experimentally by Ingard & Ising[1] for nonlinear transmission through a single orifice. The numerical liner terms are scattering acoustic energy to odd harmonics and are thus mimicking the correct physical behavior.

Duct Code Validation

The results of two trial simulations provide important checks of the duct code solution method and boundary conditions. The solution code has also been extensively tested for Kelvin-Helmholtz linear instabilities down to marginal resolutions, as discussed by Reichert[3]. Those simulations showed only slight phase and amplitude errors at resolutions of 12 to 15 points per wavelength. The present cases extend the validation to the case of well-resolved (over one hundred points per wavelength) acoustic waves. In the first case, a hard wall boundary is placed at the position of the face sheet, and the lowest duct mode (i.e., plane wave) is forced with nondimensional amplitude 0.002 (140 dB) and frequency $2\pi/17$ (2000 Hz) at the left boundary. The numerical parameters are the same as those used for the production duct simulations and are given in the following section. In this inviscid simulation, the waves should propagate along the duct with no attenuation, so sound pressure level (SPL), computed from the simulation data as

$$\text{SPL} = 10 \, log \left[\left(\frac{1}{T} \int_0^T \tilde{p}^2 \, dt \right) / \tilde{p}_{ref}^2 \right], \tag{22}$$

should remain a constant 140 dB. Here, T is a period of the wave and $\tilde{p}_{ref}$ is the nondimensional equivalent of 2×10^{-5} Pa. Further, the x-directed intensity I_x, defined by

$$I_x = \frac{1}{T} \int_0^T \tilde{u}\tilde{p} \, dt, \tag{23}$$

should be a nondimensional constant 2×10^{-6} at all points within the domain. Finally, the power transmitted along the duct per span, computed as

$$P/\text{span} = \int_0^{y_{max}} I_x \, dy, \tag{24}$$

should remain constant at 3.05×10^{-5} nondimensionally, since $y_{max} = 15.25$. It should be noted that, for the calculations of the next section, a dB drop across the duct length is also computed. For plane waves (which all later results nearly approximate), it can be shown that the dB drop between two x-stations is:

$$\text{SPL}_2 - \text{SPL}_1 = 10 \, \log f_P, \tag{25}$$

13

where f_P is the fraction of station 1 power retained at station 2. Plots of the above quantities computed from the simulation are not displayed since their profiles are flat. Examination of the numerical results, however, shows that the time-domain simulation yields the above quantities to at least four significant figures after reaching a harmonic state. This suggests that the solution method and boundary conditions are working properly for this simplified problem.

The second trial case tests the method's ability to allow waves to exit the open right boundary with minimal reflection. In this case, all significant features of the production simulations are considered, including the full duct with a liner composed of a face sheet, septum, and honeycomb. Also, a bias flow $v_{bias} = -0.01$ is applied (negative implies blowing out of the liner into the main duct). The duct is forced at the left boundary with 1250 Hz waves of 140 dB. In the first run, the domain length is 61, and in the second run, the domain length is doubled. The simulation time allows the waves to establish a harmonic state for $x \leq 61$ but does not permit them to reach the right boundary of the longer domain. This time is also long enough for reflections from the right boundary to progress back into the shorter domain. Figure 5 plots transmitted power drop per span (from the left side of the domain to the particular x-station of interest) and demonstrates that the reflections are negligible and do not degrade the solution in the interior. It is apparent that some difference between the curves exists near the outflow, though this difference is less than 3%. In this study, we use the slope of these curves in their linear region (measured arbitrarily as the slope drawn between points at $x = 18$ and $x = 36$) as one measure of duct attenuation. The two slopes are -2.295×10^{-7} and -2.297×10^{-7}, which differ by much less than 1%. It can be concluded that, for the purposes of these simulations, the artificial open boundary conditions are performing adequately.

Duct Simulation Results

The effect of varying levels of bias flow is examined for the propagation of the lowest duct mode, Eq. (18), within the lined duct of Fig. 1. The domain is discretized using a 489×155 uniform mesh ($\Delta x = \Delta y = 0.125$), and CFL numbers are approximately 0.16 ($\Delta t = 0.02$), which is about one-fourth of the numerical method's linear stability limit. The time-domain solution

14

fields are marched $6000\Delta t$ (about two duct length acoustic propagation times), at which time SPL and I_x are computed over one harmonic period. The nondimensional amplitude of the waves is set to 0.002, which corresponds to 140 dB. The frequency of the waves is $\omega = 2\pi/27.2$, which dimensionally is 1250 Hz, while bias flow is varied. Nondimensional bias flow velocities are in the range $|v_{bias}| \leq 0.03$, which dimensionally gives $|v_{bias}| \leq 10 \; m/s$. Note that this velocity is blown *out* of the liner into the main duct, so it is actually negative in value in the simulation. Other cases examine attenuation as acoustic frequency varies over a range from 630 Hz to 4000 Hz at a single bias flow level ($|v_{bias}| = 0.005$).

Figure 6 is a comparison of sound pressure levels for varying magnitudes of bias flow. The plots show SPL versus y at two x-stations. The dotted vertical lines indicate the y-locations of the two horizontal porous sheets. As expected, the SPL drops dramatically within the liner as $|v_{bias}|$ increases, especially behind the 6% septum. It is apparent that as the bias flow increases, the SPL drops most dramatically at the surface of the 6% septum sheet. This is not surprising since increasing the bias flow up to $|v_{bias}| = 0.02$ changes the resistance of this sheet from its linear value of about $0.1\rho c$ to over $5\rho c$, which nearly closes off the backing cavity. Even the face sheet attains fairly high resistance (about $0.5\rho c$) at the highest bias flow levels depicted in Fig. 6, and the SPL shows a (somewhat smaller) drop at its location also.

Another interesting feature of the SPL plots is that they flatten with increasing bias flow. With no bias flow, the SPL tends to show a broad peak near the lower wall ($y = 0$) and generally decreases with increasing y so that it is fairly low near the face sheet ($y = 15.25$). The application of bias flow generally pulls the maximum down at $y = 0$ and lifts SPL near the face sheet. The net effect is a smaller difference between maximum and minimum SPL, or a general flattening of the profile. Again, this is consistent with increasing resistance at the face sheet. As discussed in the validation section above, a hard wall placed at the face sheet, which has infinite resistance, produces completely flat profiles. Thus, it is no surprise to see flatter profiles when v_{bias} gives the face sheet a large resistance.

Recalling that the hard wall case provides no attenuation of transmitted power suggests that

$-v_{bias}$	Experimental Insertion Loss (dB)	Simulation Attenuation (dB)	Experimental f_P %	Simulation f_P %
0.0000	6.125	5.9	24.4	25.5
0.0025	8.375	9.1	14.5	12.4
0.0050	9.75	12.8	10.6	5.2
0.0075	10.50	18.1	8.9	1.5
0.0100	- 11.125	-	7.7	0.0

Table 2: Comparison of Insertion Loss and Corresponding Fractional Power at Outflow between the Present Simulation and the Experiment.

very high bias flow levels, which increase resistance and make the face sheet act more and more like a hard wall, will decrease the liner's effectiveness. Such a result is seen in Fig. 7. Plotted are transmitted power drops for four cases with increasing bias flow magnitudes. It is seen that increasing v_{bias} magnitude from 0.0 to -0.01 provides a fairly large decrease in the slope. Over the length of this duct, this provides about 40% greater drop in transmitted power. However, increasing v_{bias} magnitude from -0.01 to -0.03 provides no additional attenuation. The figure suggests that an optimum bias flow level exists for acoustic power attenuation in this lined duct configuration.

Figure 8 quantifies the optimum bias flow level more clearly. Displayed are the slopes of the transmitted power curves, in their linear region, versus bias flow magnitude. Lower (more negative) slopes indicate greater power attenuation. It appears that a bias flow $v_{bias} = -0.01$ (3.4 m/s) produces nearly optimum attenuation of transmitted acoustic power down the duct at this frequency. Larger bias flows result in a slow decrease in attenuation.

As mentioned above, the geometry of this study matches the experiment of Yu et al.,[4] so that the numerical and experimental results may be compared. The experiment measured dB insertion loss of a broadband noise source across the duct length at several single frequencies and bias flow levels. The maximum attainable bias flow magnitude in the experiment was $|v_{bias}| = 0.01$. Table 2 compares attenuations measured at 1250 Hz in the experiment, and their corresponding fraction f_P of transmitted power remaining by outflow, with the same quantities computed in the present study. Both the experiment and present simulation exhibit the same trend of dramatic attenuation, followed by a decreasing return, with increasing $|v_{bias}|$.

Another comparison with the experiment is depicted in Fig. 9. Values of the simulation's attenuation over the duct length (computed according to Eq. (25)), for $v_{bias} = -0.005$, are shown at several plane wave frequencies ($600\ Hz \leq f \leq 4000\ Hz$) in the top plot, while the bottom plot is insertion loss as measured in the experiment. The same frequency response trends are evident in both plots: peak attenuation is present at about 1250 Hz with fairly dramatic fall off to either side. Note that, on a linear scale, differences when attenuation is 10 dB or more are quite small. The approximately 3 dB difference in peak attenuation (at 1250 Hz) corresponds to an experimentally observed 95% and a numerically calculated 90% power attenuation. Again, the simulation agrees favorably with experiment.

Concluding Comments

This study has developed a promising new method for predicting noise attenuation in acoustically lined ducts. The method is founded upon time-domain governing equations which are modified to account for the presence of acoustic lining materials interior to the domain. The modification is simply a source term in the momentum equations which provides for acoustic reactance and both linear and nonlinear acoustic resistance, but in the time-domain. The modified equations may be readily time integrated using numerical methods. The main benefit of analyzing duct problems in this way is that complicated liner behavior and structure are easily implemented. Also, multiple frequency and multiple mode noise environments may be examined. In sum, the method developed here provides promise as an analysis technique for actual liner structures within realistic noise environments.

The time-domain analysis is empirical in the sense that constants in the modified governing equations must be matched to complex impedance data for the component sheets of the liner using a numerical impedance tube. The impedance tube simulations employ the same equation modifications, and the model constants are adjusted until the standing wave pattern in the tube matches that which would be produced by a sample with the desired complex impedance. A one-to-one correspondence exists between the frequency-domain impedance values and the time-domain model constants, which aids in the matching process. Spectral analysis of the pressure

17

signal transmitted through the impedance tube sample gives the same scattering to odd harmonics seen in experiment. The matched constants are then used in the full duct simulations to mimic the behavior of that material sample.

Two-dimensional numerical simulations involving a lined duct provide additional evidence that the liner model is a viable design tool. The computational geometry matches that of an experiment conducted at Rohr, Inc. The trends observed in the simulations compare well with those of the experiment. Specifically, attenuation as a function of bias magnitude at a single frequency, and attenuation as a function of frequency at a single bias magnitude, behave the same in the experiment and simulation. The quantitative agreement is acceptable in light of experimental uncertainty, the numerical model's empiricism, and the numerical restriction to two dimensions. It is found that, for this liner and 140 dB waves of 1250 Hz, an optimal bias flow magnitude is about 0.01, or 3.4 m/s. With the optimum bias velocity, the liner efficiency is significantly improved over the no bias liner, lending support to the idea that bias flow may be used to tune and improve the performance of a liner. Further, this application demonstrates that the new model may be used as a design tool for determining optimal liner configurations and operating conditions.

Acknowledgments

References

1. Ingard, U. & Ising, H. Acoustic Nonlinearity of an Orifice. *J. Acoustical Society of America.* 42(1), 6-17 (1967).

2. Melling, T.H. The Acoustic Impedance of Perforates at Medium and High Sound Pressure Levels. *J. Sound and Vibration.* 29(1), 1-65 (1973).

3. Tam, C.K.W. & Auriault, L. Time-Domain Impedance Boundary Conditions for Computational Aeroacoustics. *AIAA J.* 34(5), 917-923 (1996).

4. Yu, J., Kwan, H.W., & Stockham, T. Advanced Aeroacoustic Nacelle Program. NASA Contract Report for Contract NAS1-20102, Task 9 (1996).

5. Motsinger, R.E. & Kraft, R.E. Design and Performance of Duct Acoustic Treatment. Chapter 14 in *Aeroacoustics of Flight Vehicles: Theory and Practice*, NASA RP-1258.

6. Nayfeh, A.H., Kaiser, J.E., & Telionis, D.P. Acoustics of Aircraft Engine-Duct Systems. *AIAA Journal.* 13(2), 130-153 (1975).

7. Morse, P.M. & Ingard, K.U. *Theoretical Acoustics.* Princeton University Press. pp.252-254 (1968).

8. Zorumski, W.E. & Parrott, T.L. Nonlinear Acoustic Theory for Thin Porous Sheets, in *Progress of NASA Research Relating to Noise Alleviation of Large Subsonic Jet Aircraft.* NASA SP-189, 17-27 (1968).

9. Zorumski, W.E. & Parrott, T.L. Nonlinear Acoustic Theory for Rigid Porous Materials. NASA TN D-6196 (1971).

10. Gottlieb, D. & Turkel, E. Dissipative Two-Four Methods for Time-Dependent Problems. *Mathematics of Computation.* 30(136), 703-723 (1976).

11. Thompson, K.W. Time Dependent Boundary Conditions for Hyperbolic Systems. *J. Computational Physics.* 68, 1-24 (1987).

12. Thompson, K.W. Time-Dependent Boundary Conditions for Hyperbolic Systems, II. *J. Computational Physics.* 89, 439-461 (1990).

13. Kinsler, L.E., Frey, A.R., Coppens, A.B., & Sanders, J.V. *Fundamentals of Acoustics.* New York: John Wiley & Sons. pp.204-206 (1982).

14. Reichert, R.S. *Numerical Simulation of Compressible Flows with Application to Noise Control.*

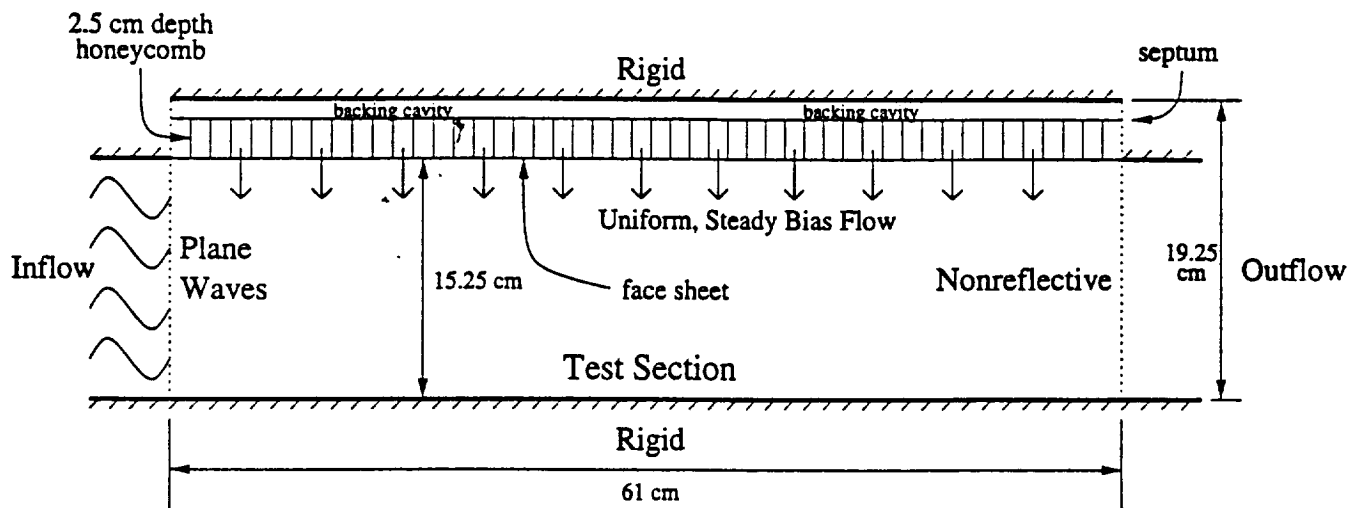   Ph.D. Thesis, University of Colorado (1998).
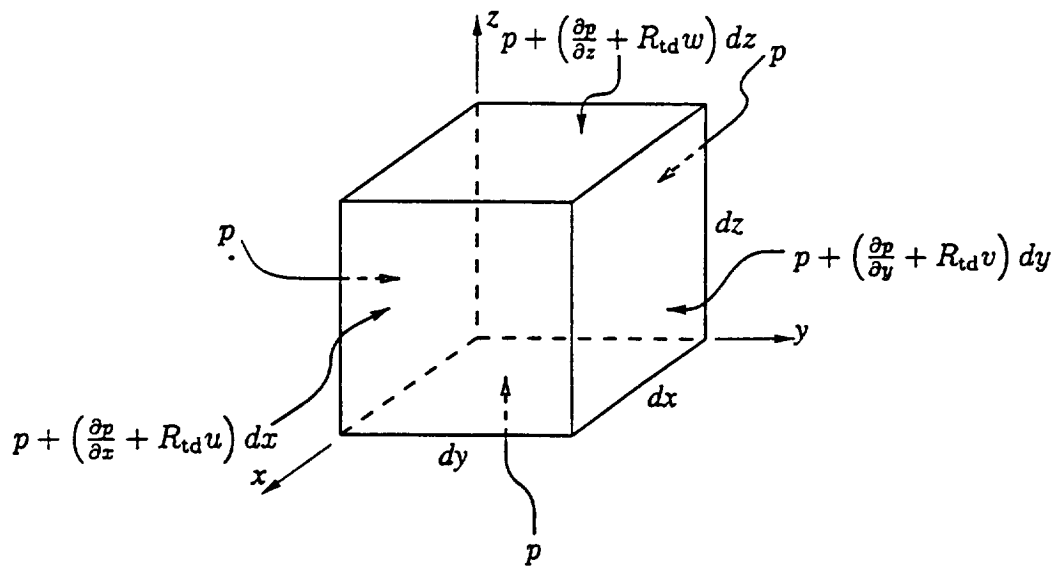
Figure 1: Duct Test Section Geometry

Figure 2: Control Volume Containing Distributed Lining Material
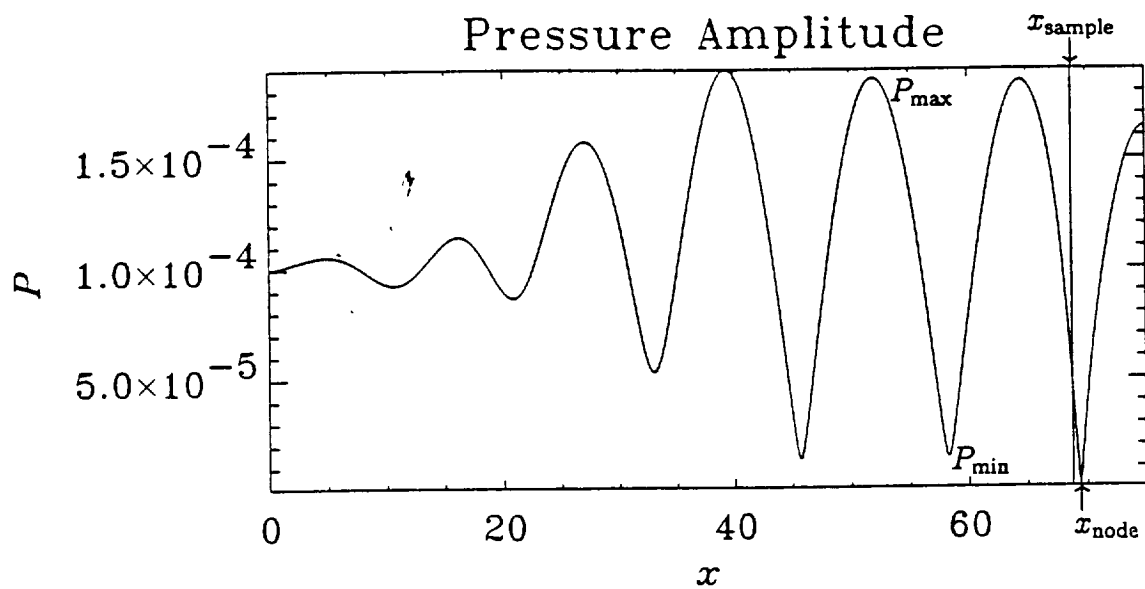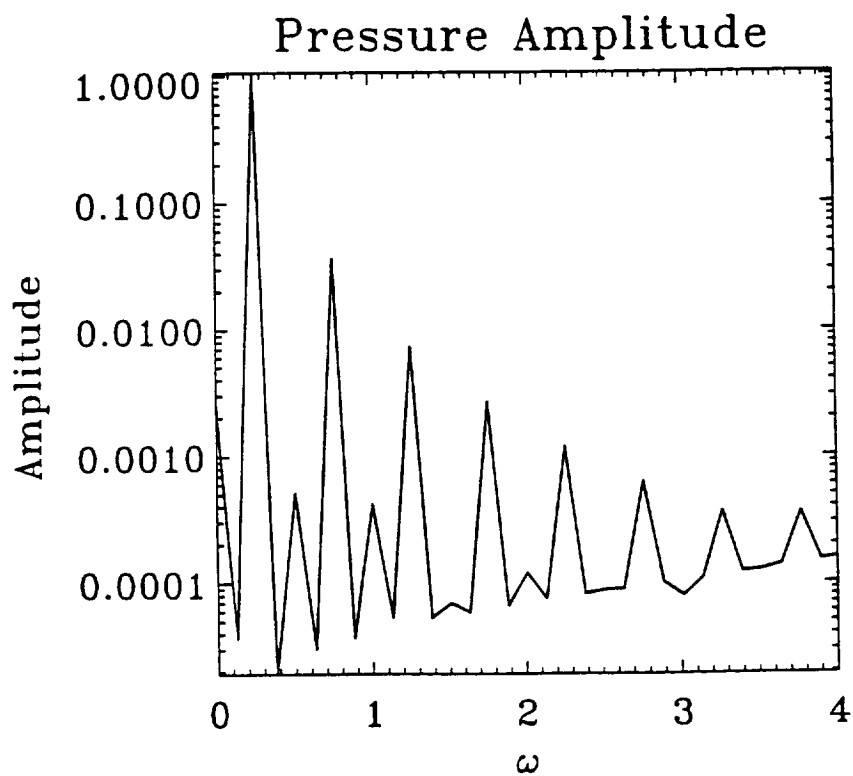
21

Figure 3: Numerical Impedance Tube Solution

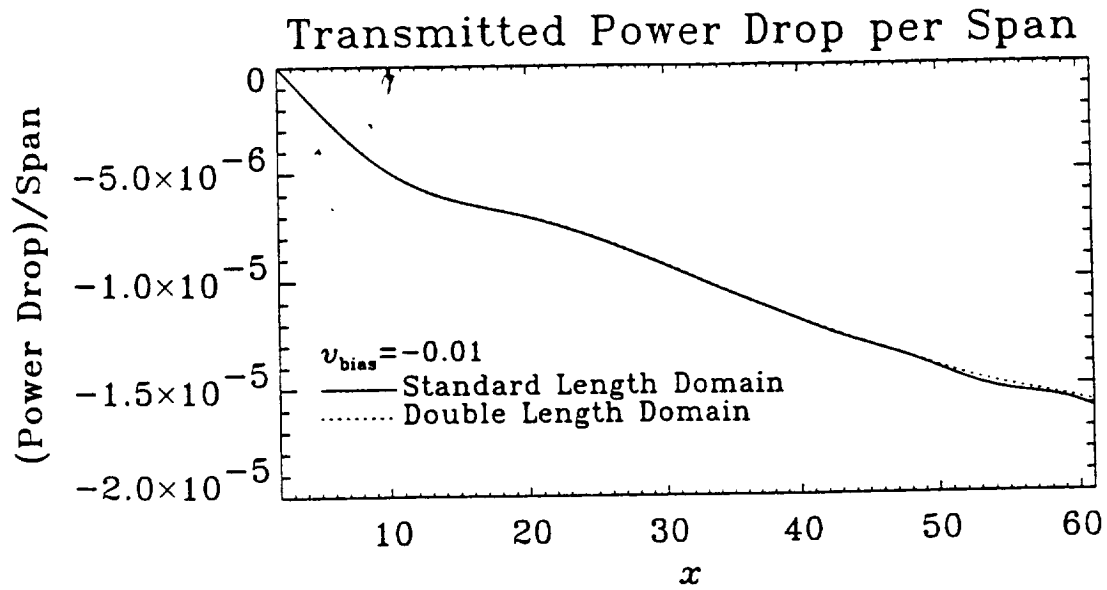Figure 4: Spectrum of Pressure Time Series between Sample and Rigid Termination in Impedance Tube

22

Transmitted Power Drop per Span

Figure 5: Axial Power per Span Drop from Left Boundary: Short vs. Long Domain
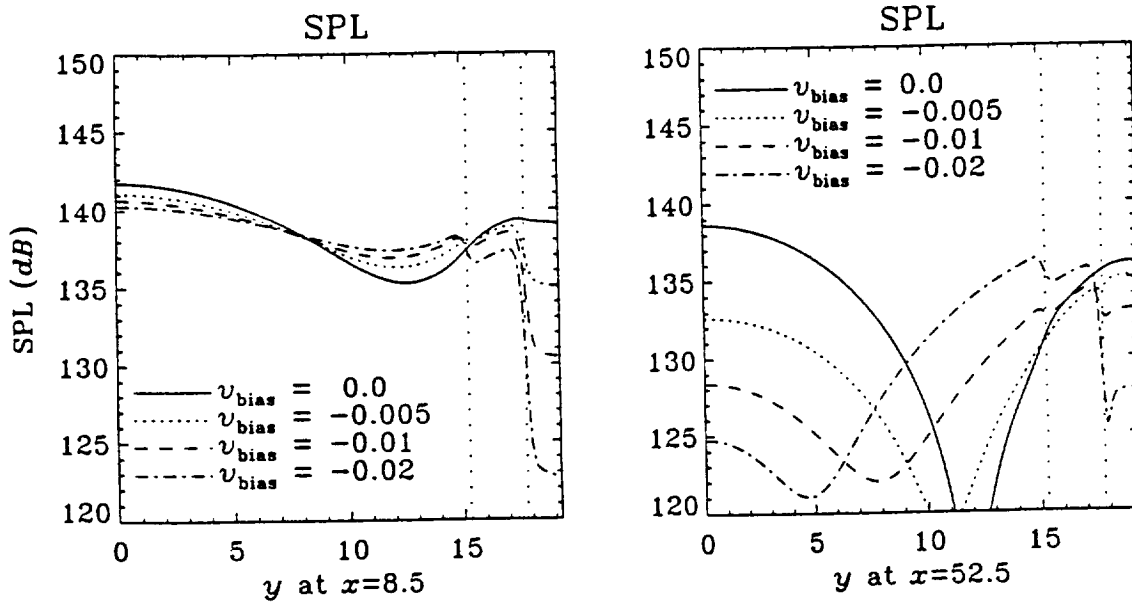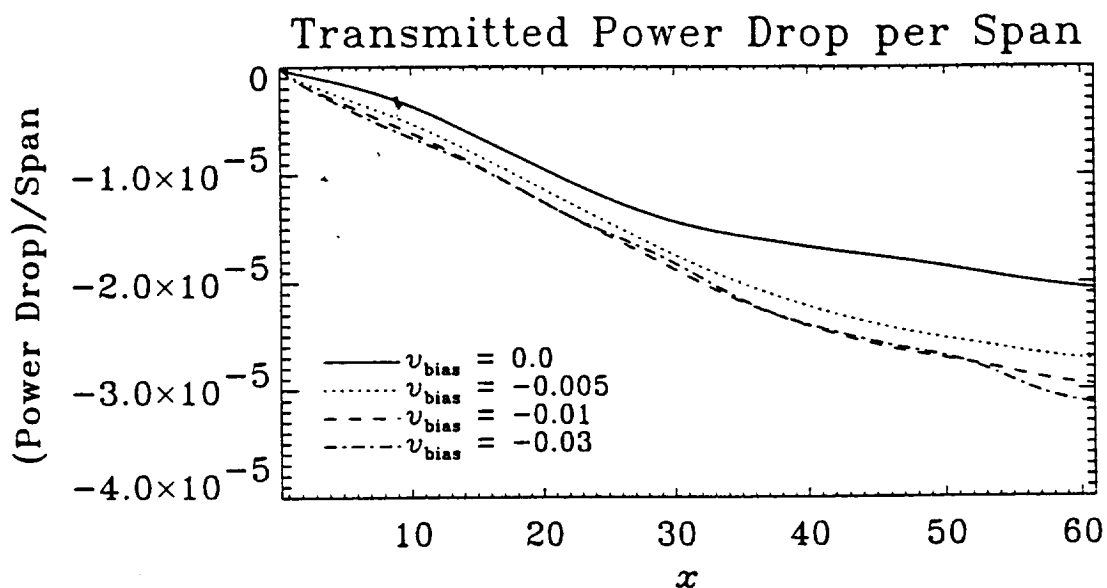

Figure 6: SPL Levels for Increasing Bias Flow Magnitudes

23

Transmitted Power Drop per Span

Figure 7: Axial Power per Span Drop for Increasing Bias Flow Magnitudes
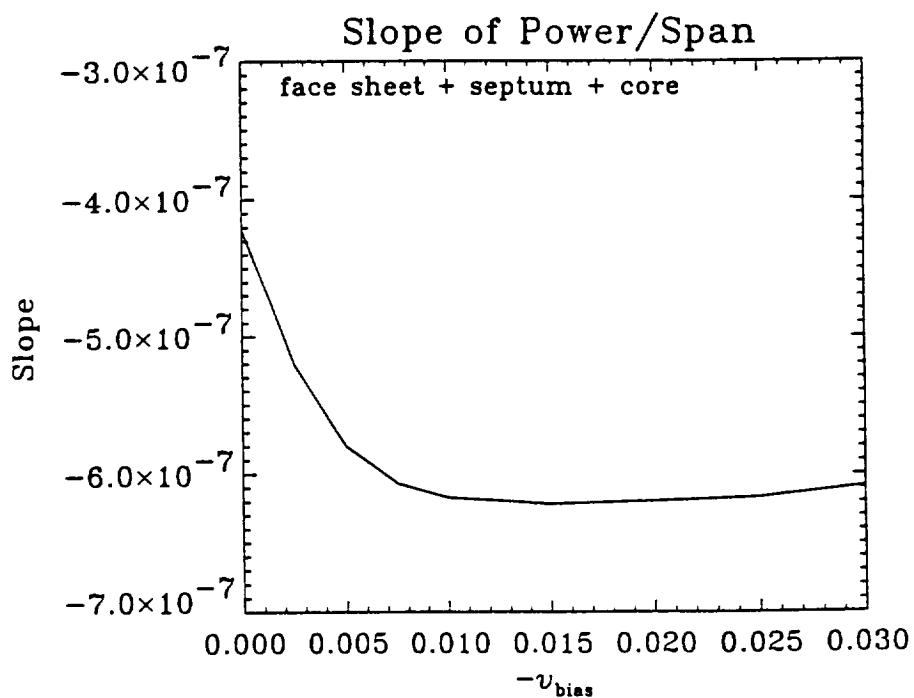
Slope of Power/Span

Figure 8: Slope of Axial Power per Span in Linear Region for Three Liner Configurations

24

Relative Power Drop

$v_{bias}=-0.005$

Power Drop (dB)

Present Results

f(Hz)

Experimental Insertion Loss

$v_{bias}=-0.005$

Insertion Loss (dB)

Yu, Kwan, and Stockham
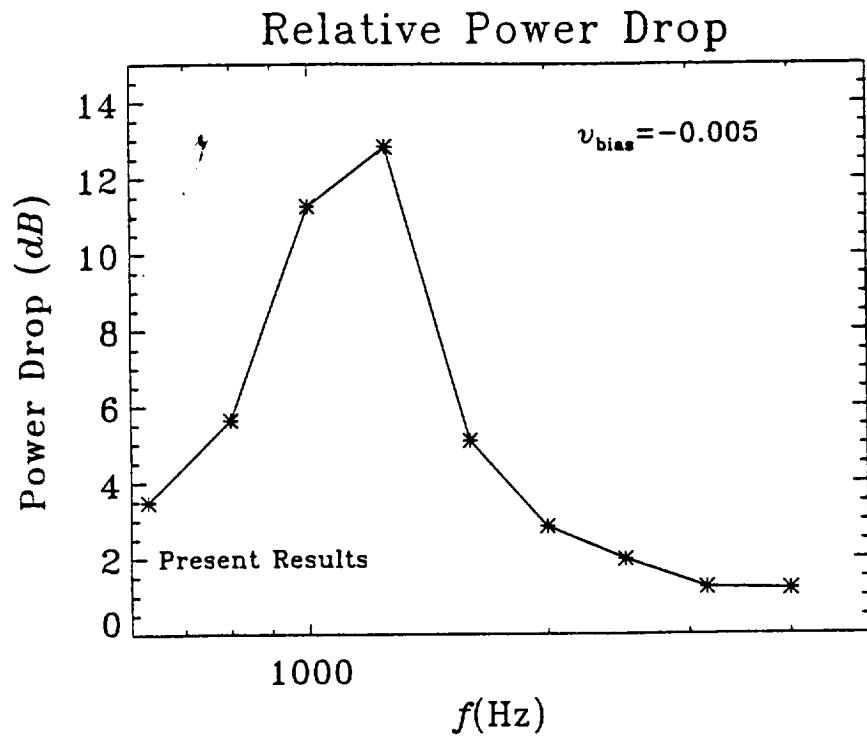Rohr, Inc.

f (Hz)
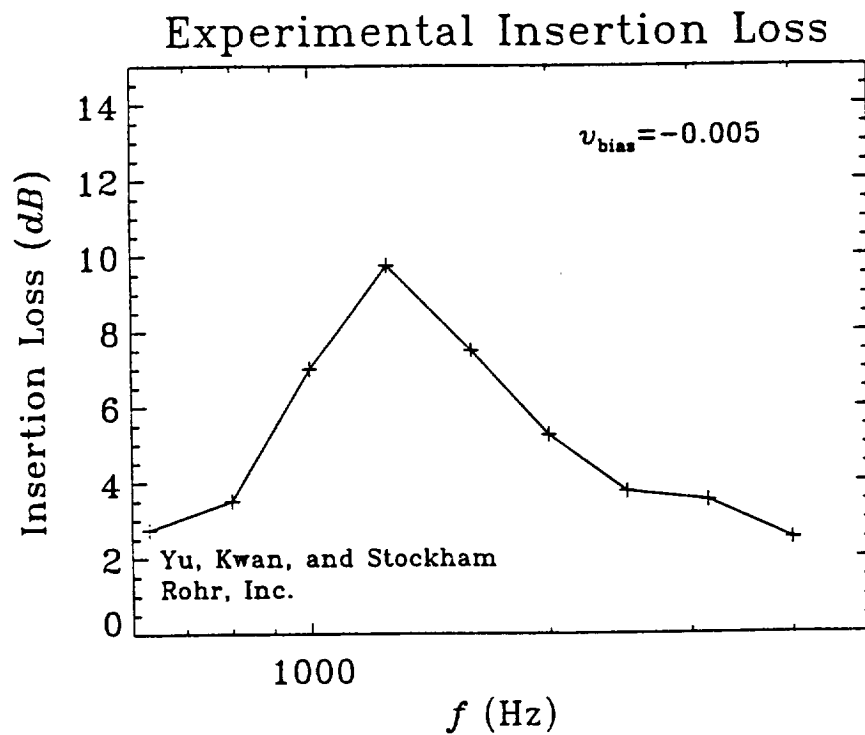
Figure 9: Attenuation Frequency Response Comparison: Simulation and Experiment

25

TIME-DOMAIN SIMULATION OF
ACOUSTIC PROPAGATION IN A LINED DUCT

R.S. Reichert[*] and S. Biringen[†]
Department of Aerospace Engineering Sciences
University of Colorado
Boulder, Colorado 80309-0429

Abstract

An inviscid, spatial time-domain numerical simulation is employed to compute acoustic wave propagation in a duct treated with an acoustic liner. The motivation is to assess the effects on sound attenuation of bias flow passed through the liner for application to noise suppression in jet engine nacelles. Physically, the liner is composed of porous sheets with backing air cavities. The mathematical model lumps the sheets' presence into a continuous empirical source term which modifies the right-hand side of the momentum equations. This source term specifies the time-domain behavior of the frequency-domain resistance and reactance of the liner's component sheets. The source term constants are matched to frequency-domain impedance data via a one-dimensional numerical impedance tube simulation. Nonlinear behavior of the liner at high sound pressure levels is included in the form of the source term. Sound pressure levels and axially transmitted power are computed to assess the effect of various magnitudes of bias flow on attenuation. Simulation results are compared to available experimental data on a geometrically similar lined duct.

Problem Introduction and Description

Reduction of noise emitted from jet engines continues to be a key component of aircraft design. One major facet is inlet noise. Mechanical and hydrodynamic noise from the engine components propagates upstream and out of the inlet. Current generation jet engine designs treat nacelle inlets with acoustic liners composed of porous sheets with backing air cavities for acoustic attenuation. It is well known that the impedance of porous sheets varies at high sound pressure levels. Observations show that incident sound pressure amplitude relates nonlinearly to particle velocity both for a single orifice (Ingard[1]) and porous sheets (Melling[2]). One concept for varying the impedance properties of liners is to exploit this nonlinear behavior by blowing a low level, steady bias flow through them. In this concept, the bias flow, which might be generated naturally by redirecting the oncoming stream through the nacelle skin, could be adjusted to tune the liner impedance for optimum attenuation over a range of flight conditions. The present study considers high amplitude acoustic propagation within a simple duct geometry in an effort to model the physics and eventually validate this idea.

The goal of this work is to develop a design tool for time-domain numerical simulation of acoustics in the presence of sound-absorbing liners with bias flow. The physical and geometric attributes of the liners are lumped into a model term with empirical constants. This model term modifies the governing equations such that the liner manifests itself *interior* to the domain rather than through finite impedance *boundary conditions*. The model constants are matched to complex impedance data for liner materials so that the simulation produces the same impedance behavior as the actual material. The governing equations are integrated forward in time to capture the evolution of the acoustic field in the presence of the liner structure. The primary motivation is to assess and optimize the effect of natural bias flow through the liner.

The geometry considered here approximates that of a lined duct test section constructed at Rohr, Inc., as detailed in Yu, Kwan, & Stockham[3]. Depicted in Fig. 1, the section is 19.25 *cm* in height and 61 *cm* in length. The numerical simulation considers a two-dimensional planar cut bounded by solid rigid walls at top and bottom and by open boundaries, indicated by dotted lines in the figure, at left and right. The top surface of the duct is acoustically treated with a liner composed of a porous face

527

sheet (18% open area) and backing septum (6% open area) sandwiching a honeycomb core. Additionally, the air cavity behind the septum may contain backing sheets (8.7% open area). These sheets approximate the presence of corrugation septa which are distributed in the duct's *third* dimension in the actual experiment; two configurations distributing the septa in the simulation's *two* dimensions were tested, as will be discussed. Plane waves (i.e., lowest duct modes) are forced at the left boundary and allowed to propagate along the duct to the right through a quiescent air medium.

Development of Time-Domain Model Form

Consider the integral form of inviscid conservation of momentum applied to a fixed control volume,

$$\int_V \frac{\partial(\rho\vec{v})}{\partial t}\, dV = -\int_A (\rho\vec{v}\cdot d\vec{A})\,\vec{v} - \int_A p\, d\vec{A}, \quad (1)$$

which states that the rate of change of momentum within the control volume is equal to the net flow of momentum across the volume's surface plus the momentum change due to surface pressure forces. Suppose now that we apply this equation to the Cartesian differential control volume ($\lim_{\Delta V \to 0} \Delta V = dV = dx\, dy\, dz$) depicted in Fig. 2. Further, suppose that some porous acoustic lining material is distributed uniformly throughout the volume. The material's presence will lead to a pressure change across the volume in each coordinate direction, augmenting the pressure gradient as shown. The pressure force term becomes

$$\lim_{\Delta V \to 0} -\int_A p\, d\vec{A} = -\frac{\partial p}{\partial x_i}\, dV - \left(\frac{\Delta p}{dx}\right)_i dV, \quad (2)$$

where we have employed tensor notation on the right side. Following Zorumski & Parrott[4,5], we write this pressure jump term as a time-domain resistive term R_{td} multiplying the local velocity u_i,

$$\left(\frac{\Delta p}{dx}\right)_i = R_{td} u_i, \quad (3)$$

so that

$$\lim_{\Delta V \to 0} -\int_A p\, d\vec{A} = -\frac{\partial p}{\partial x_i}\, dV - R_{td} u_i\, dV. \quad (4)$$

Equation (3) assumes that the pressure jump will instantaneously satisfy a steady flow resistance relation across the differential volume. Additionally, the effective fluid density within the volume is reduced by a constant time-domain factor X_{td} between 0 and 1 due to the material presence:

$$\rho \longrightarrow X_{td}\rho \qquad 0 < X_{td} \leq 1. \quad (5)$$

For the differential control volume, the momentum flux term becomes:

$$\lim_{\Delta V \to 0} -\int_A (\rho\vec{v}\cdot d\vec{A})\,\vec{v} = X_{td}\frac{\partial}{\partial x_j}(\rho v_i v_j)\, dV. \quad (6)$$

Substituting Eqs. (4), (5), and (6) into Eq. (1) and recovering vector notation yields a modified differential momentum equation:

$$\frac{\partial(\rho\vec{v})}{\partial t} + \nabla \cdot (\rho\vec{v}\,\vec{v}) = -\frac{1}{X_{td}}(\nabla p - R_{td}\vec{v}). \quad (7)$$

We must now substitute model relations for R_{td} and X_{td} which properly mimic the time-domain behavior of acoustic lining materials.

Mathematical Model

The governing equations are the two-dimensional Euler equations, which express conservation of mass, momentum, and energy for the inviscid motion of compressible fluids. They are here written for a Cartesian domain with no body forces present:

$$\frac{\partial\vec{W}}{\partial t} + \frac{\partial\vec{F}}{\partial x} + \frac{\partial\vec{G}}{\partial y} = \vec{S}, \quad (8)$$

where

$$\vec{W} = (\rho \quad \rho u \quad \rho v \quad E)^T, \quad (9)$$

and

$$\vec{F} = \begin{pmatrix} \rho u \\ \rho u^2 \\ \rho v u \\ [E+p]u \end{pmatrix}, \qquad \vec{G} = \begin{pmatrix} \rho v \\ \rho u v \\ \rho v^2 \\ [E+p]v \end{pmatrix}. \quad (10)$$

The state equation closes the system:

$$E = \frac{p}{\gamma - 1} + \frac{1}{2}\rho(u^2 + v^2). \quad (11)$$

The above set has, as the dependent variables, the conserved quantities of mass ρ, x-directed momentum ρu, y-directed momentum ρv, and total energy E, each expressed on a per volume basis. The primitive variables are density ρ, x-directed velocity u, y-directed velocity v, and pressure p. Specification of the open sides as nonreflective and the solid walls as rigid slip boundaries completes the definition of the mathematical problem.

We have nondimensionalized the equation system using the following reference scales:

$$
\begin{aligned}
l_r &= 0.01\ m &\longrightarrow&\quad \text{length scale,} \\
U_r &= 340.25\ m/s &\longrightarrow&\quad \text{velocity scale,} \\
l_r/U_r &= 2.939 \times 10^{-5}\ s &\longrightarrow&\quad \text{time scale,} \\
\rho_r &= 1.225\ kg/m^3 &\longrightarrow&\quad \text{density scale,} \\
\rho_r U_r^2 &= 1.418 \times 10^5\ Pa &\longrightarrow&\quad \text{pressure, energy scale.}
\end{aligned}
$$

528

Note that the density and velocity reference values correspond to standard atmosphere density and sound speed. It is also worth noting that the equations will capture both linear and nonlinear phenomena.

The presence of the discrete porous sheets is felt via the source term $\vec{S}$ from the right hand side of Eq. (7). We form R_{td} and X_{td} to capture the general experimental frequency-domain behavior observed by Ingard[1], Melling[2], and Zorumski & Parrott[5]. Specifically, Rohr, Inc. provided impedance data in the form

$$z = (\mathcal{R}_0 + \mathcal{S}V) + i\mathcal{X}, \tag{12}$$

where V is the root-mean-square velocity at the sheet surface. The real part is the velocity dependent resistance, and the imaginary part is the reactance. The term $\vec{S}$ allows for simple nonlinear behavior in the resistance:

$$\vec{S} = -\frac{1}{1 - X(f_X(x,y)/[f_X(x,y)]_{max})}$$

$$\times \begin{pmatrix} 0 \\ [\partial p/\partial x + u f_R(x,y)(A + B|u|)] \\ [\partial p/\partial y + v f_R(x,y)(A + B|v|)] \\ 0 \end{pmatrix}$$

$$- \begin{pmatrix} 0 \\ u\ C(x,y) \\ 0 \\ 0 \end{pmatrix}. \tag{13}$$

The empirical parameters A, B, and X respectively specify the levels of linear resistance, nonlinear resistance, and linear reactance of each sheet, but in the time-domain. The distribution $C(x,y)$ is set to a constant value ($C = 0.8$) between the face sheet and parallel backing septum to account for the presence of the honeycomb core. Since this additional resistance-like term only appears in the x-momentum equation, it acts to suppress u within the core and thus helps the face sheet/septum combination approximate a locally reacting liner surface. Note that $A = B = C = X = 0$ gives back the original Euler equations, so these correspond to open air. The functions $f_R(x,y)$ and $f_X(x,y)$ control the spatial distribution of the liner's effect for the resistance and reactance, respectively. They are specified as Gaussian distributions in a coordinate s normal to the sheet surfaces:

$$f(s) = \frac{1}{\sigma}\frac{1}{\sqrt{2\pi}}e^{-s^2/2\sigma^2}. \tag{14}$$

The constant σ_R is fixed as $2\Delta x$ simply to distribute the discrete effect of sheet resistance for numerical purposes. The constants A, B, X, and σ_X are matched to complex impedance data via a numerical impedance tube simulation, as described below. The authors conducting the duct experiment[3] provided the impedance data.

Nonlinear behavior in reactance is not explicitly modeled in Eq. (13). This nonlinearity tends to reduce the sheet reactance, but the effect is not indefinite in the provided impedance data. When the root-mean-square normal velocity at the sheet surface attains a high enough level, the reactance again assumes a constant value. The velocity at which this saturation occurs depends on the particular sheet porosity, but is at most 0.0095 for the component sheets considered here. A *constant* reactance must be used for all sheets when $|v_{bias}| \geq 0.0095$. Below this level, each sheet must be considered separately as to whether its reactance behaves nonlinearly or is saturated.

It was found in the course of the simulations that if an explicit nonlinear reactance term is used in Eq. (13), the model produces a smaller reactance reduction than it should. This resulted in large jumps in the averaged data (i.e., in the slope of the transmitted power per span curves seen in Fig. 7) when the bias flow magnitude dictated that the reactance switch from nonlinear to saturated levels. Of course, this only affected cases for which $|v_{bias}| \leq 0.0095$, since all of the sheets perform with saturated reactance for $|v_{bias}| > 0.0095$. To approximate the variable reactance, X was computed to be a fixed number between the linear X_{max} and the saturated X_{min}, sized according to the expected normal velocity at each sheet surface. Effectively, this process is a linearization of the reactance about each particular bias flow level.

Numerical Solution Method

We wish to discretize and integrate the partial differential equation system (8), coupled with the spatial boundary conditions. The domain is rectangular, with uniform mesh in both the x- and y-directions. The time-advancement scheme is Gottlieb & Turkel's[6] explicit (2,4) scheme, which is second-order accurate in time and fourth-order in space. The variant of the method used here is a MacCormack-like explicit predictor/corrector. For grids that are uniform in x and y, the method may be written as:

529

$$\vec{W}_{i,j}^* = \vec{W}_{i,j}^n$$
$$-\lambda_x[7(\vec{F}_{i+1,j}^n - \vec{F}_{i,j}^n) - (\vec{F}_{i+2,j}^n - \vec{F}_{i+1,j}^n)]$$
$$-\lambda_y[7(\vec{G}_{i,j+1}^n - \vec{G}_{i,j}^n) - (\vec{G}_{i,j+2}^n - \vec{G}_{i,j+1}^n)]$$
$$+\Delta t(\vec{D})_{i,j}^n + \Delta t(\vec{S})_{i,j}^n, \qquad (15)$$

$$\vec{W}_{i,j}^{n+1} = \frac{1}{2}\Big\{\vec{W}_{i,j}^n + \vec{W}_{i,j}^*$$
$$-\lambda_x[7(\vec{F}_{i,j}^* - \vec{F}_{i-1,j}^*) - (\vec{F}_{i-1,j}^* - \vec{F}_{i-2,j}^*)]$$
$$-\lambda_y[7(\vec{G}_{i,j}^* - \vec{G}_{i,j-1}^*) - (\vec{G}_{i,j-1}^* - \vec{G}_{i,j-2}^*)]$$
$$+\Delta t(\vec{D})_{i,j}^* + \Delta t(\vec{S})_{i,j}^*\Big\}. \qquad (16)$$

Here,

$$\lambda_x = \frac{\Delta t}{6\Delta x}, \qquad \lambda_y = \frac{\Delta t}{6\Delta y}.$$

The above steps employ forward differencing in the predictor step and backward differencing in the corrector step. This is switched on alternating time steps to a predictor with backward differencing and corrector with forward differencing in order to obtain the full (2,4) accuracy. For stability, the Courant-Friedrichs-Lewy (CFL) number should satisfy:

$$CFL_x = \frac{(u+a)_{\max}\Delta t}{\Delta x} < \frac{2}{3},$$

and

$$CFL_y = \frac{(v+a)_{\max}\Delta t}{\Delta y} < \frac{2}{3},$$

where a is the local sound speed, $a = \sqrt{\gamma p/\rho}$.

The (2,4) stencil has five points in both x- and y-directions, so it extends over the domain edges at a boundary and first interior point. The method uses the unmodified (2,4) scheme at the first interior point. To account for the point beyond the edge, fluxes are extrapolated (third-order) to a ghost point one increment outside the domain. Boundary points are treated with the method of Thompson[7,8]. This boundary treatment uses a characteristic decomposition of the Euler equations to give an estimate of the flux derivative normal to the boundary at the boundary.

Artificial viscosity terms may be added to the scheme to enhance stability, as indicated by the $\vec{D}$ terms above. Sixth-order dissipation is added as a source term to the right-hand side of the Euler equations:

$$\vec{D} = \epsilon_d\left((\Delta x)^6\frac{\partial^6\vec{W}}{\partial x^6} + (\Delta y)^6\frac{\partial^6\vec{W}}{\partial y^6}\right). \qquad (17)$$

The sizes of the artificial viscosity terms are $O[(\Delta x)^6]$ and $O[(\Delta y)^6]$, so the fourth-order spatial accuracy of the method is unaffected. The parameter ϵ_d is user-defined and did not exceed $\epsilon_d = 0.04$. The central difference coefficients used for the sixth-derivatives are computed using Lagrange polynomials. We found some explicit dissipation necessary to suppress spurious oscillations developing around the porous sheets.

The mean bias flow is specified as a "frozen" field upon which the acoustic perturbations are allowed to evolve. In this way, the mean field need not be computed; nor does it evolve. The addition of a forcing term $\vec{\epsilon}$ to Eq. (8) accomplishes this:

$$\frac{\partial\vec{W}}{\partial t} + \frac{\partial\vec{F}}{\partial x} + \frac{\partial\vec{G}}{\partial y} - \vec{S} + \vec{\epsilon} = 0, \qquad (18)$$

where

$$\vec{\epsilon} = -\frac{\partial\overline{\vec{F}}}{\partial x} - \frac{\partial\overline{\vec{G}}}{\partial y} + \overline{\vec{S}}. \qquad (19)$$

The overbar here denotes the mean field. A uniform vertical velocity v_{bias} is used throughout the domain for the mean field. Thus, the bias is directed normal to the liner, and there is no grazing flow. This technique has the limitation that the mean field does not feel the presence of the liner structure, but it is a quick way to obtain a converged bias flow.

Numerical Impedance Tube Simulation

As mentioned above, the liner model's empirical parameters must be matched to the impedance data for the porous sheets under consideration. To this end, a numerical model of an impedance tube was developed. One-dimensional Euler equations are integrated on a domain with a rigid termination at the right end. The left boundary is forced with acoustic waves. A numerical porous sheet "sample" is placed some distance to the left of the rigid termination by centering the Gaussian distributions (14) at that point. The effective impedance of the sample is deduced from the standing wave pattern set up by the incident and reflected waves.

Details of the impedance computation may be found in introductory acoustics texts. Here, we follow that of Kinsler, Frey, Coppens, & Sanders[9]. The measured impedance z is computed as

$$z = \frac{1 + Ke^{i\theta}}{1 - Ke^{i\theta}}. \qquad (20)$$

The constant K is given in terms of the standing wave ratio SWR, the ratio of maximum to minimum pressure amplitude:

$$K = \frac{\text{SWR} - 1}{\text{SWR} + 1}, \quad \text{where} \quad \text{SWR} = \frac{P_{\max}}{P_{\min}}. \qquad (21)$$

530

The value for θ is given by the phase of the standing waves relative to the sample surface:

$$\theta = 2k(x_{sample} - x_{node}) - \pi, \qquad (22)$$

where k is the wavenumber of the incident waves. The impedance value thus measured equals that of the sample plus the impedance of the closed tube behind the sample. Kinsler et al.[9] show that this backing tube impedance is $-\cot(kd)$, where d is the depth of the cavity from the sample to the rigid termination. Consequently, we fix the depth at one-quarter incident wavelength such that $-\cot(kd) = 0$, so that the measured impedance is simply that of the sample.

The time-domain constants A, B, X, and σ_X are adjusted until the computed impedance matches that of the porous sheet, which is of the form of Eq. (12). The present model has a simple nonlinear frequency-domain behavior, but there is no inherent limitation to the complexity that could be mimicked with a time-domain model. In matching, there exists a one-to-one correspondence between A and $\mathcal{R}_0$, B and $\mathcal{S}$, and X and $\mathcal{X}$. The parameter σ_X may also be adjusted to effect gross changes in $\mathcal{X}$. Figure 3 shows a representative standing wave solution for the 6% open sheet, with the center of the sheet indicated by the vertical line. The following table shows the constants obtained through application of this method to the three different sheet types.

Por.	A	B	$X_{\max}$	$X_{\min}$	σ_X
18.0%	0.0235	20.5	0.705	0.535	4.0 Δx
8.7%	0.0428	96.1	0.705	0.535	6.8 Δx
6.0%	0.06	193.5	0.78	0.605	8.8 Δx

This method is general in the sense that complex impedance data for any sample, porous sheet or other, can be matched to the empirical constants of the model.

Duct Code Validation

The results of two trial simulations provide important checks of the duct code solution method and boundary conditions. In the first case, a hard wall boundary condition is placed at the position of the face sheet, and the lowest duct mode is forced with nondimensional amplitude 0.002 (140 dB) and frequency $2\pi/17$ (2000 Hz) at the left boundary. In this inviscid simulation, the waves should propagate along the duct with no attenuation, so sound pressure level (SPL), computed from the simulation data as

$$SPL = 10\, log\left[\left(\frac{1}{T}\int_0^T \bar{p}^2\, dt\right)/\bar{p}_{ref}^2\right], \qquad (23)$$

should remain a constant 140 dB. Here, T is a period of the wave and $\bar{p}_{ref}$ is the nondimensional equivalent of 2×10^{-5} Pa. Further, the x-directed intensity I_x, defined by

$$I_x = \frac{1}{T}\int_0^T \bar{u}\bar{p}\, dt, \qquad (24)$$

should be a nondimensional constant 2×10^{-6} at all points within the domain. Finally, the power transmitted along the duct per span, computed as

$$P/\text{span} = \int_0^{y_{max}} I_x\, dy, \qquad (25)$$

should remain constant at 3.05×10^{-5} nondimensionally, since $y_{max} = 15.25$. Plots of the above quantities as computed from the simulation are not displayed since all profiles are flat. Examination of the numerical results, however, show that the time-domain simulation yields the above quantities to at least four significant figures after reaching a harmonic state.

The second trial case tests the method's ability to allow waves to exit the open right boundary with minimal reflection. In this case, all significant features of the simulations are included. That is, the full domain is considered, including the presence of a liner with face sheet, septum, and honeycomb. Also, a bias flow $v_{bias} = -0.01$ is applied. One run employs the domain length of 61 to be used for the later simulations; the domain length is doubled for the second run. The time of simulation is designed so that the waves have a chance to establish a harmonic state for $x \le 61$ but do not have a chance to reach the right boundary of the long domain. The time is also long enough for reflections to appear in the shorter domain. Figure 4 demonstrates that degradation from reflections is slight. Plotted are drops in transmitted power per span from the left side of the domain to the particular x-station of interest. It is apparent that some difference between the curves exists near the outflow, though this difference is less than 3%. In this study, we use the slope of these curves in their linear region (measured arbitrarily as the slope drawn between points at $x = 22$ and $x = 35$) to quantify the duct attenuation. The two slopes are -2.035×10^{-7} and 2.034×10^{-7}, which differ by less than 1%. It can be concluded that for the purposes of these simulations, the artificial open boundary conditions are performing adequately.

Duct Simulation Results

The effect of varying levels of bias flow is examined for the propagation of the lowest duct mode

531

when the liner consists of the face sheet and parallel septum sandwiching a honeycomb core. The domain is discretized using a 489×155 uniform mesh ($\Delta x = \Delta y = 0.125$), and CFL numbers are approximately 0.16, which is about one-fourth of the linear stability limit. The nondimensional amplitude of the waves is set to 0.002, which corresponds to 140 dB. The frequency of the waves is $\omega = 2\pi/17$, which dimensionally is 2000 Hz. Nondimensional bias flow velocities are in the range $0.001 \leq |v_{bias}| \leq 0.03$, which dimensionally gives 0.34 $m/s \leq |v_{bias}| \leq 10$ m/s.

Figure 5 is a comparison of sound pressure levels for varying magnitudes of bias flow. The plots show SPL cuts in y at two x-stations. The y-location of the two horizontal porous sheets is indicated by the dotted vertical lines. As expected, SPL drops dramatically within the liner as $|v_{bias}|$ increases. It is apparent that as the bias flow increases, SPL drops more dramatically at the surface of the 6% septum sheet. This is sensible because increasing bias flow up to $|v_{bias}| = 0.02$ changes the resistance of this sheet from its linear value of about $0.1\rho c$ to over $5\rho c$, which essentially closes off the backing cavity. Even the face sheet attains fairly high resistance (about $0.5\rho c$) at the highest bias flow levels depicted in Fig. 5, and SPL shows a (somewhat smaller) drop at its location also.

Another interesting feature of the SPL plots is that they flatten with increasing bias flow. With no bias flow, SPL tends to show a broad peak near the lower wall ($y = 0$) and generally decreases with increasing y so that it is fairly low at the face sheet ($y = 15.25$). The application of bias flow generally pulls the maximum down at $y = 0$ and lifts SPL near the face sheet. Again, this is consistent with increasing resistance at the face sheet. As discussed in the validation section above, a hard wall placed at the face sheet, which is infinite resistance, produces completely flat profiles. Thus, it is no surprise to see fairly flat profiles when v_{bias} gives the face sheet a large resistance.

Recalling that the hard wall case provided no attenuation of transmitted power suggests that very high bias flow levels, which make the face sheet act more and more like a hard wall, will decrease the liner's effectiveness. Such a result is seen in Fig. 6. Plotted are transmitted power drops for four cases with increasing bias flow magnitudes. It is seen that increasing v_{bias} from 0.0 to -0.01 provides a fairly large decrease in the slope. Over the length of this duct, this provides about 30% greater drop in transmitted power. However, increasing v_{bias} from -0.01 to -0.02 provides no additional attenuation. The figure suggests an optimum bias flow level for acoustic

power attenuation in this duct/liner configuration.

Figure 7 quantifies the optimum bias flow level more clearly. Displayed are the slopes of the transmitted power curves in their linear region versus bias flow magnitude. Lower slopes indicate greater power attenuation. The first plot exhibits slopes for the basic configuration of an 18% face sheet plus 6% parallel backing septum with an empty backing cavity. For the second plot, cases were run with 8.7%, $\pm 45°$ corrugation sheets present in the backing cavity, but running in the x-direction. Finally, cases for the third plot were run with an 8.7% parallel septum present in the backing cavity midway between the 6% septum and the rigid wall. The latter two configurations are attempts to, in some measure, account for the presence of 8.7% sheet corrugations distributed in the *third* dimension of the actual experimental duct lining[3]. All cases include the honeycomb between the face sheet and septum. It is seen in Fig. 7 that the presence of 8.7% sheets in the backing cavity only marginally affects the minimum slope. For all three configurations, it appears that a bias flow $v_{bias} = -0.01$ (3.4 m/s) produces optimum attenuation of transmitted acoustic power down the duct at this frequency.

As mentioned above, the geometry of this study matches the experiment of Yu et al.[3] The experiment measured dB insertion loss of a broadband noise source across the duct length at several different frequencies and bias flow levels. The following table compares attenuations measured at 2000 Hz in the experiment to the power slopes computed in the present study:

$-v_{bias}$	Experiment Insertion Loss (dB)	Simulation Power Slope ($\times 10^{-7}$)
0.0000	3.50	-1.35
0.0025	4.25	-1.60
0.0050	5.25	-1.70
0.0075	5.25	-1.80
0.0100	4.75	-1.85
0.0125	–	-1.85
0.0250	–	-1.75

Both the experiment and present simulations exhibit the same trend of rapidly increasing attenuation, followed by slowly decreasing attenuation, with increasing $|v_{bias}|$. The optimum v_{bias} in the experiment has a somewhat lower magnitude, but overall, the agreement is favorable.

Another comparison is depicted in Fig. 8. Values of the simulation's power slope for $v_{bias} = -0.005$ are shown at several different plane wave frequencies in the upper plot, while the lower plot shows

532

insertion loss as measured in the experiment. The same frequency response trends are evident in both plots: peak attenuation is present at about 1250 Hz with fairly dramatic fall off to either side. Again, the simulation agrees favorably with experiment.

Concluding Comments

This study has developed a new method for predicting noise attenuation in acoustically lined ducts. Time-domain simulation with governing equations modified to include the time-domain behavior of liner resistance and reactance was applied to a duct test section geometry. A liner configuration composed of a face sheet and parallel septum surrounding a honeycomb core of depth 1.25 cm was set on one side of the 15.25 cm duct. A cavity of depth 2.75 cm backed the septum; distribution of additional septa within this backing cavity produced minimal change in the results. The time-domain liner model included nonlinear behavior in the resistance of the liner's component sheets. The simulations have demonstrated the presence of an optimum bias flow level. For waves of 140 dB and frequency 2000 Hz propagating axially along the duct, $|v_{bias}| = 3.4$ m/s produced the greatest attenuation in transmitted acoustic power along the duct. Trends with varying bias flow and varying frequency agreed favorably with experimental measurements performed at Rohr, Inc.

Acknowledgments

References

1. Ingard, U. Acoustic Nonlinearity of an Orifice. *J. Acoustical Society of America.* 42(1), 6-17 (1967).

2. Melling, T.H. The Acoustic Impedance of Perforates at Medium and High Sound Pressure Levels. *J. Sound and Vibration.* 29(1), 1-65 (1973).

3. Yu, J., Kwan, H.W., & Stockham, T. Advanced Aeroacoustic Nacelle Program. NASA Contract Report for Contract NAS1-20102, Task 9 (1996).

4. Zorumski, W.E. & Parrott, T.L. Nonlinear Acoustic Theory for Thin Porous Sheets, in *Progress of NASA Research Relating to Noise Alleviation of Large Subsonic Jet Aircraft.* NASA SP-189, 17-27 (1968).

5. Zorumski, W.E. & Parrott, T.L. Nonlinear Acoustic Theory for Rigid Porous Materials. NASA TN D-6196 (1971).

6. Gottlieb, D. & Turkel, E. Dissipative Two-Four Methods for Time-Dependent Problems. *Mathematics of Computation.* 30(136), 703-723 (1976).

7. Thompson, K.W. Time Dependent Boundary Conditions for Hyperbolic Systems. *J. Computational Physics.* 68, 1-24 (1987).

8. Thompson, K.W. Time-Dependent Boundary Conditions for Hyperbolic Systems, II. *J. Computational Physics.* 89, 439-461 (1990).

9. Kinsler, L.E., Frey, A.R., Coppens, A.B., & Sanders, J.V. *Fundamentals of Acoustics.* New York: John Wiley & Sons. pp.204-206 (1982).
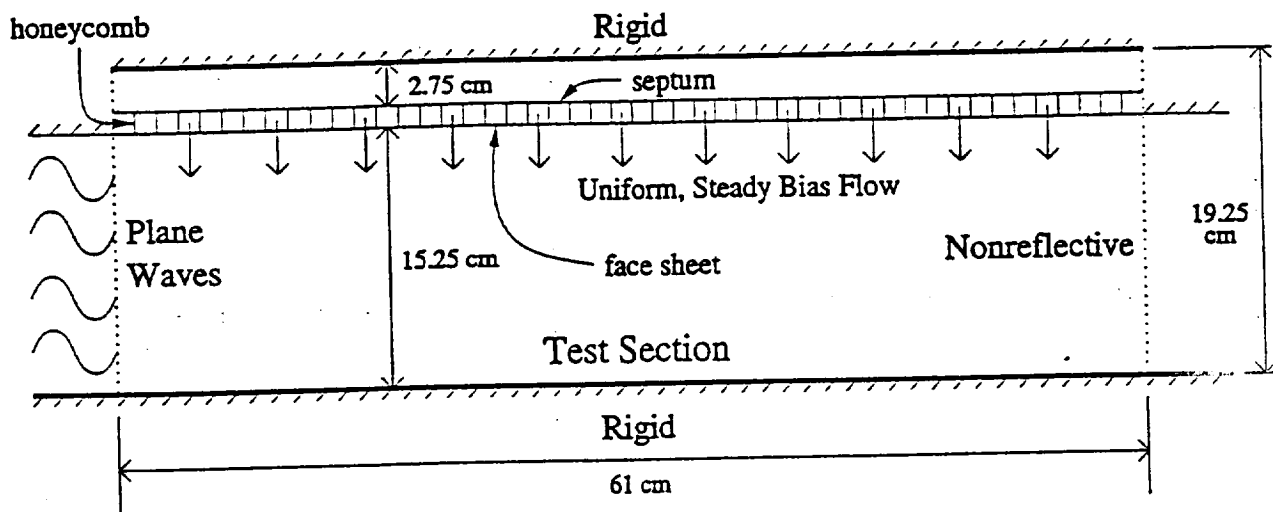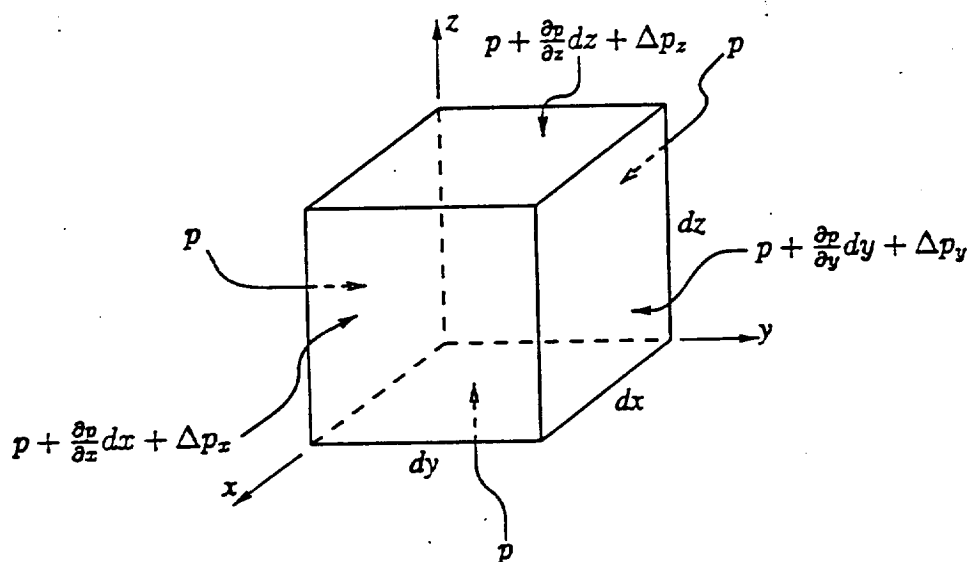
Figure 1: Duct Test Section Geometry

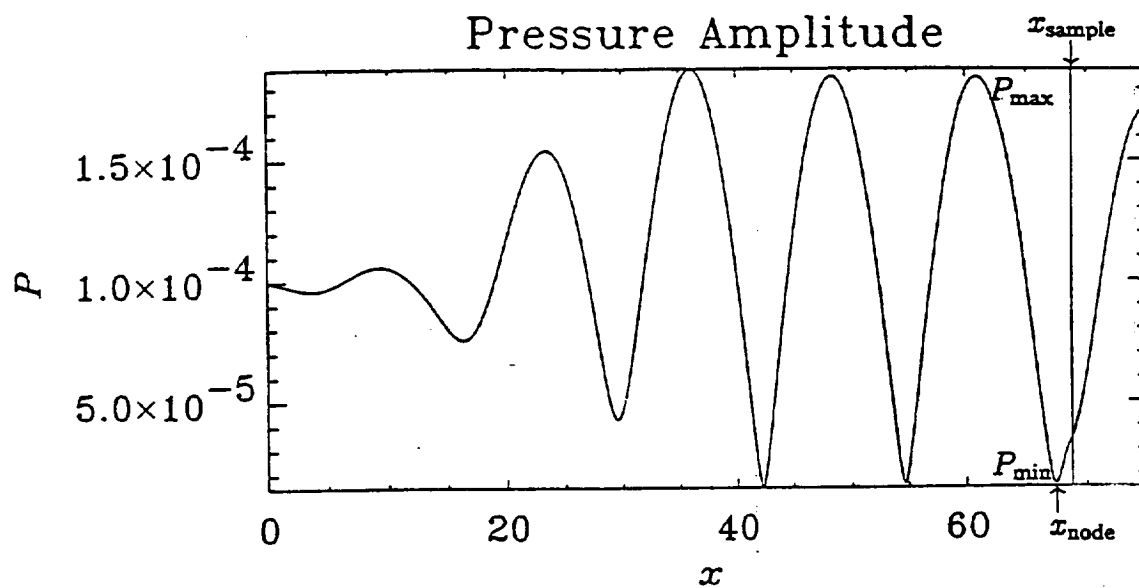Figure 2: Control Volume Containing Distributed Lining Material

534

Pressure Amplitude

Figure 3: Numerical Impedance Tube Solution
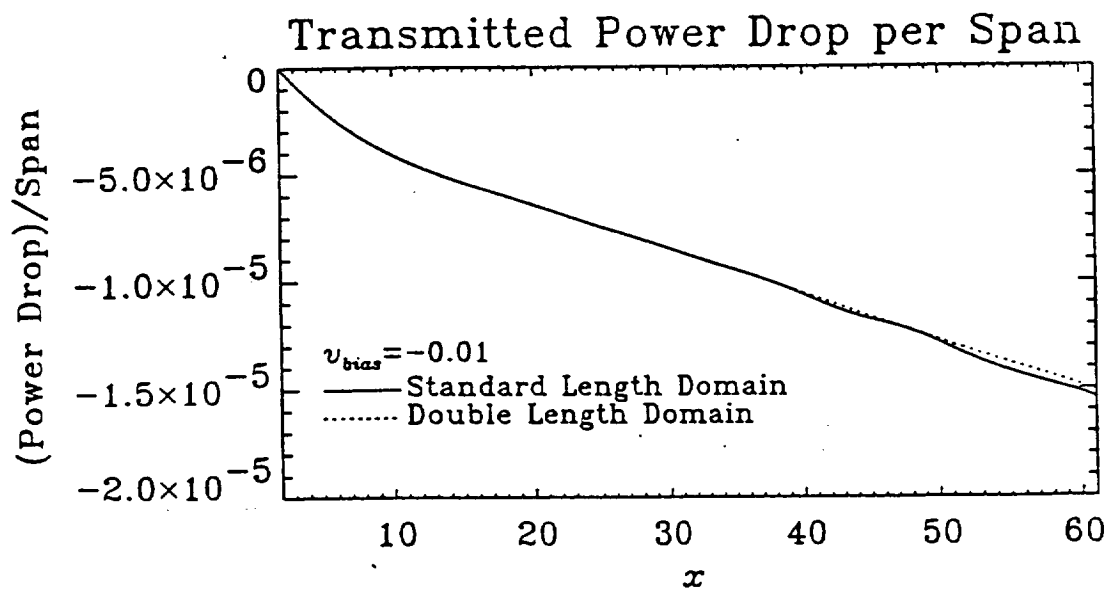
Transmitted Power Drop per Span

Figure 4: Axial Power per Span Drop from Left Boundary: Short vs. Long Domain
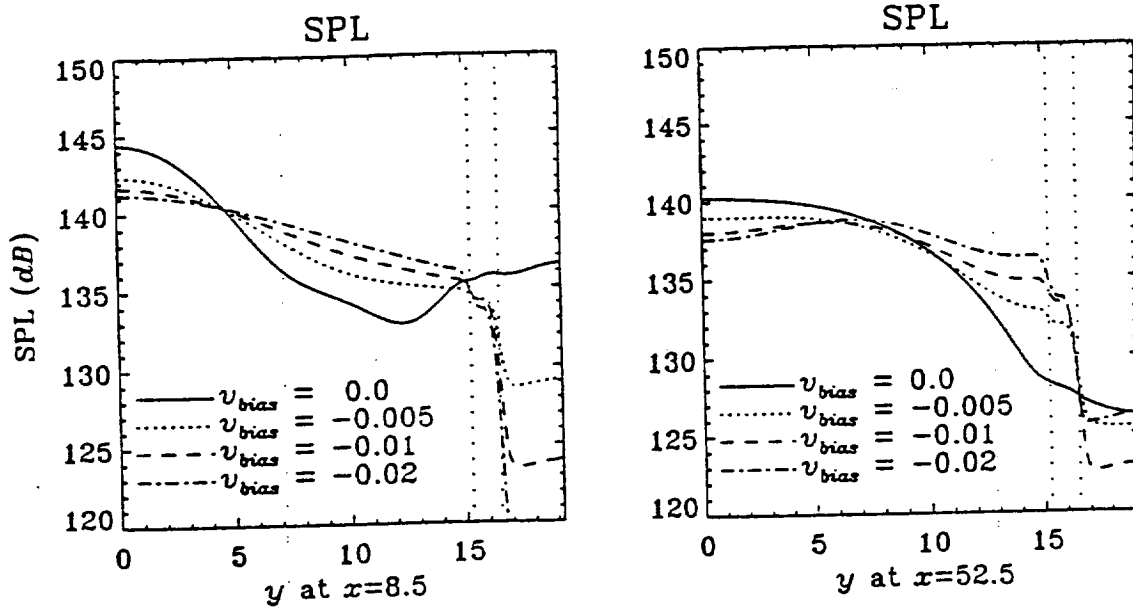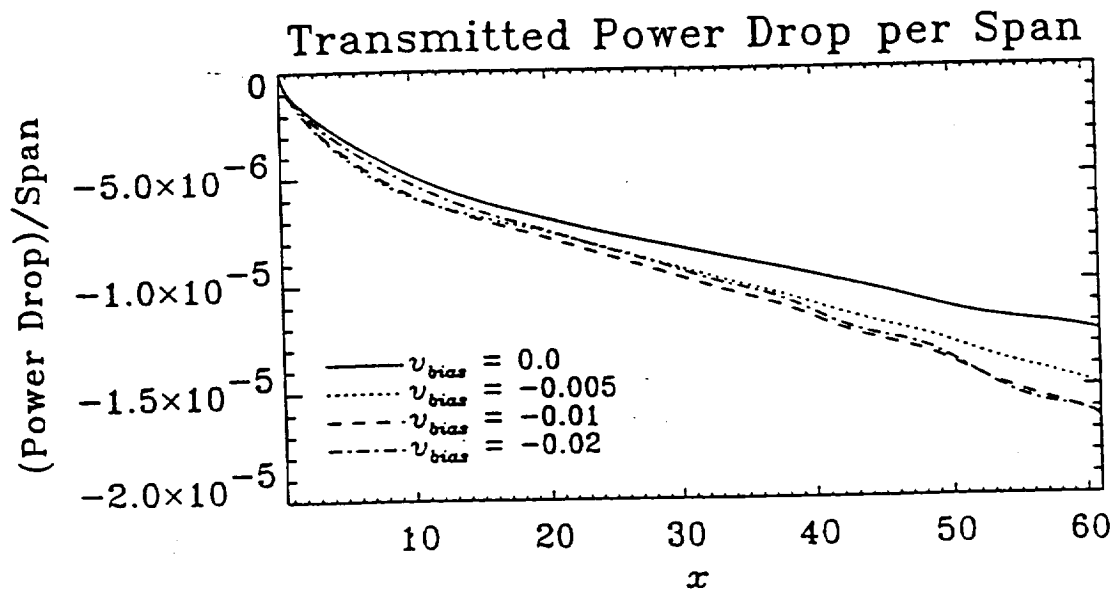
Figure 5: SPL Levels for Increasing Bias Flow Magnitudes

Figure 6: Axial Power per Span Drop for Increasing Bias Flow Magnitudes

Slope of Power/Span

face sheet + septum + core

Slope of Power/Span

face sheet + septum + core
+ backing corrugations

Slope of Power/Span

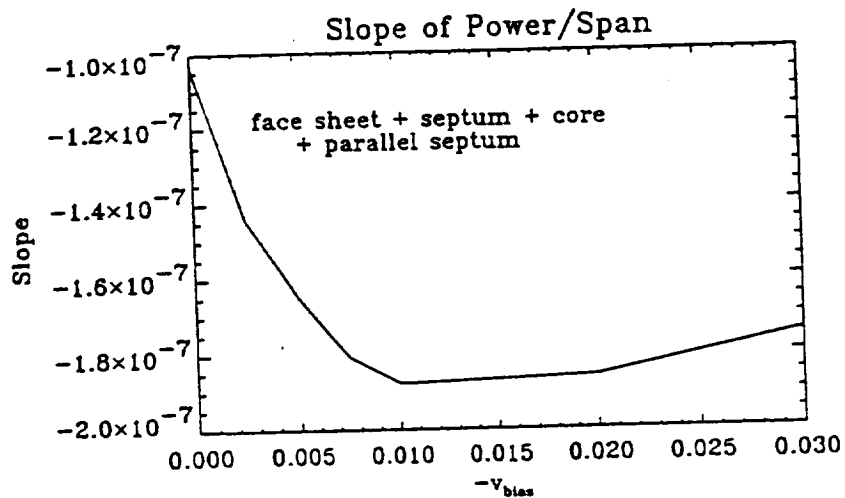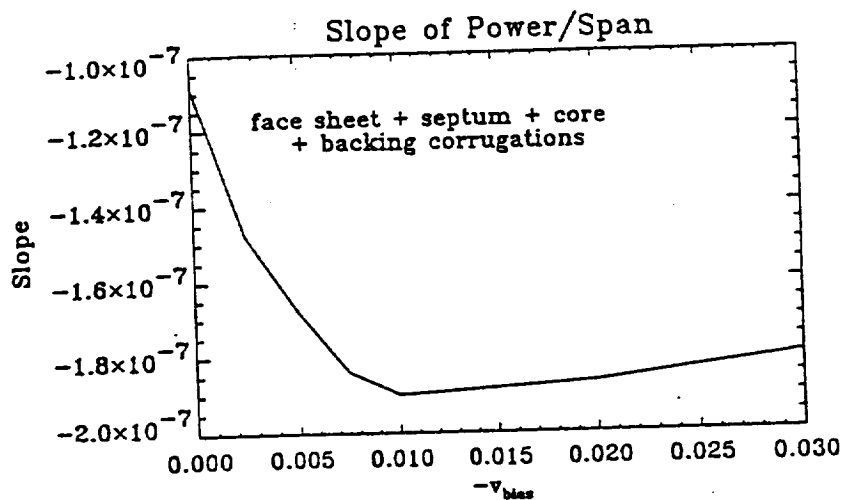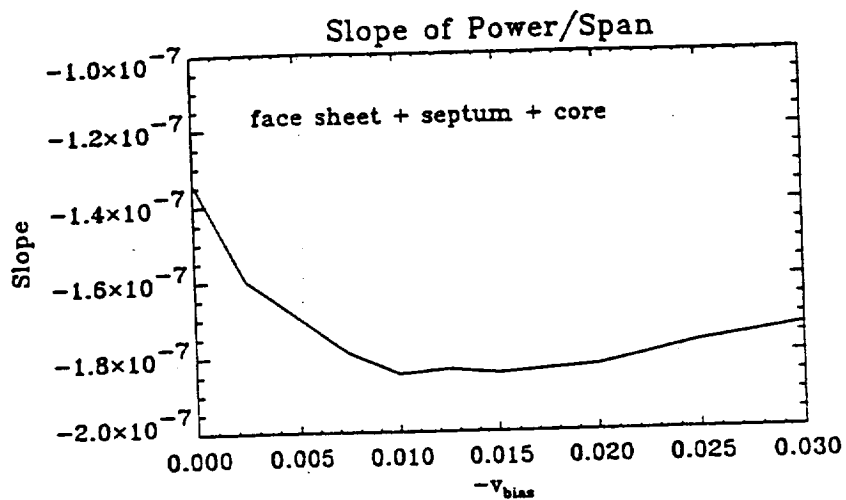face sheet + septum + core
+ parallel septum

Figure 7: Slope of Axial Power per Span in Linear Region for Three Liner Configurations

537

Numerical Slope: Power/Span

face sheet + septum + core
$v_{bias}=-0.005$

-(Slope)

4.0×10^{-7}

3.0×10^{-7}

2.0×10^{-7}

1.0×10^{-7}

0

Present Results

1000

$f(\text{Hz})$

Experimental Insertion Loss

face sheet + septum + core
$v_{bias}=-0.005$

Insertion Loss (dB)

10

8

6

4

2

0

Yu, Kwan, and Stockham
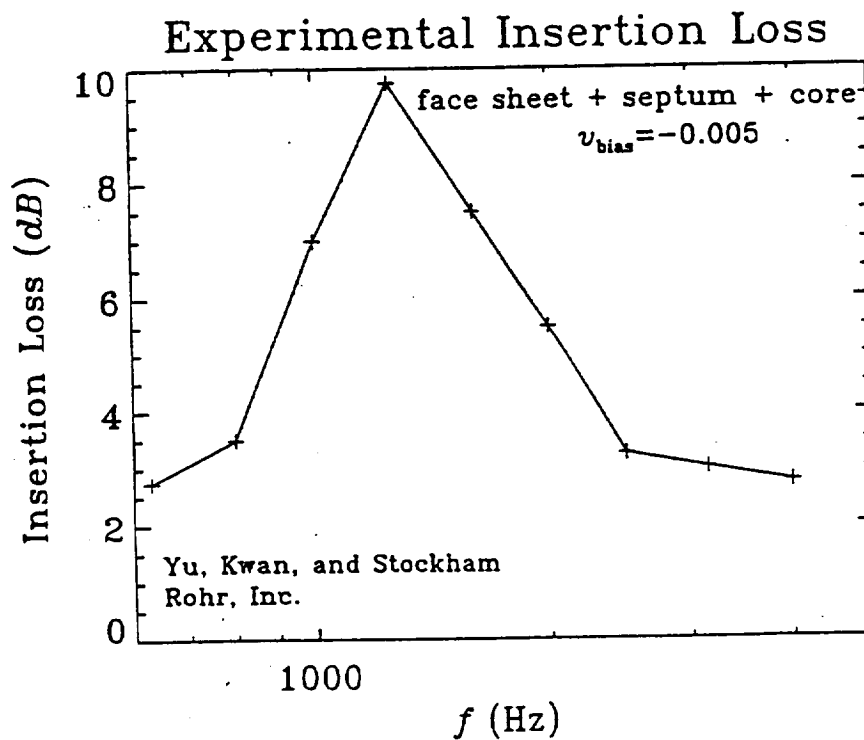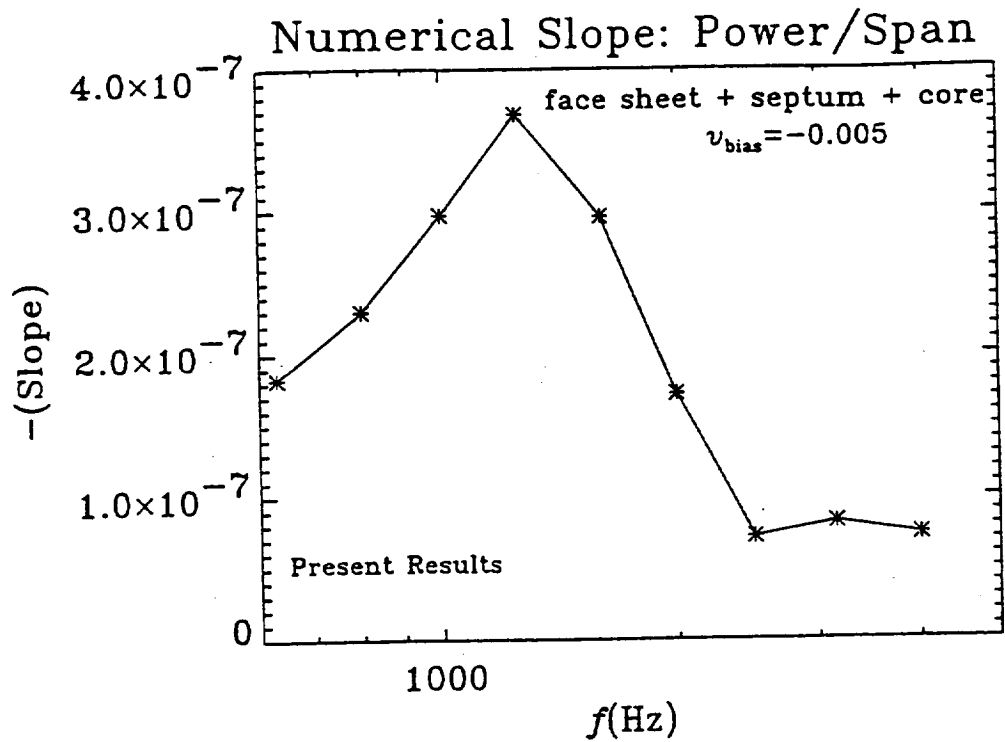Rohr, Inc.

1000

f (Hz)

Figure 8: Attenuation Frequency Response Comparison: Simulation and Experiment